iScience

CellPress
OPEN ACCESS

Article

Optic atrophy 1 mediates muscle differentiation by promoting a metabolic switch via the supercomplex assembly factor SCAF1

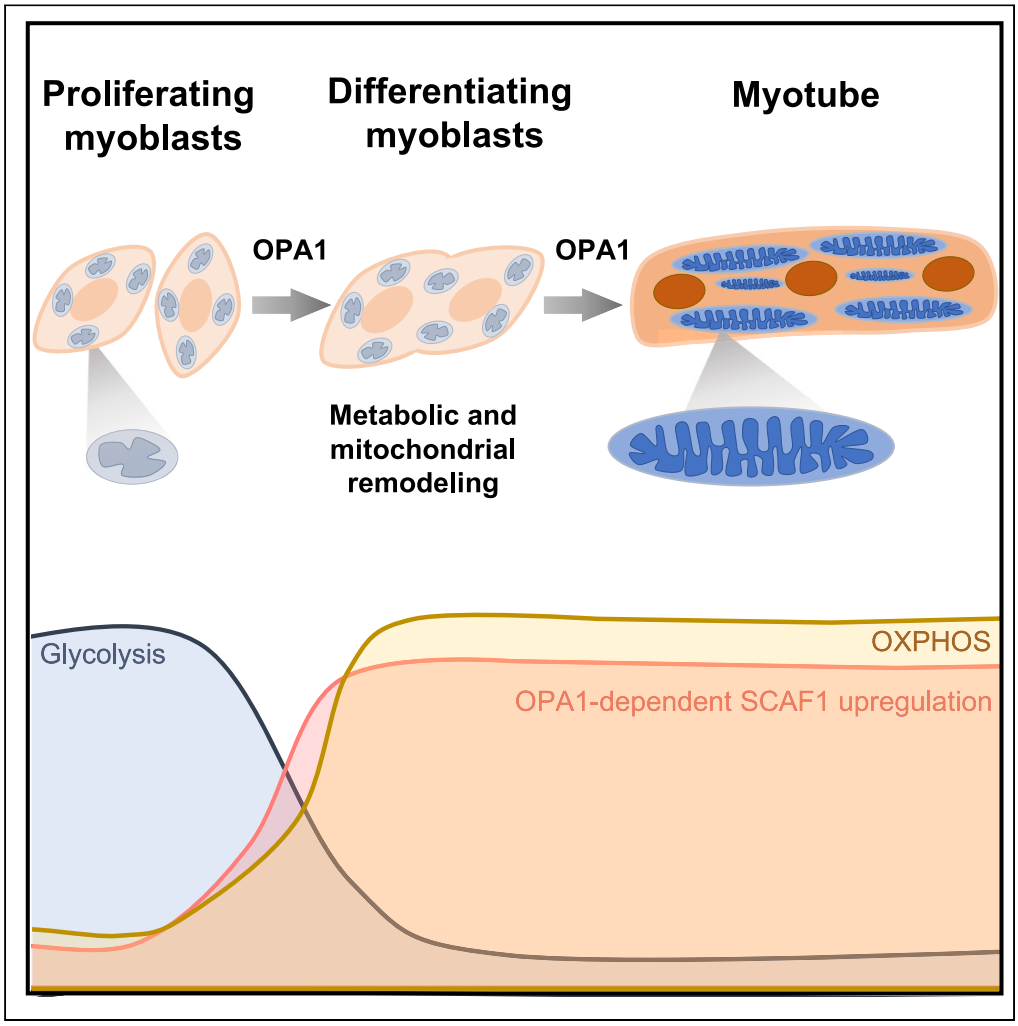

Matthew Triolo, Nicole Baker, Soniya Agarwal, Nikita Larionov, Tina Podinić, Mireille Khacho

mkhacho@uottawa.ca

Highlights

Mitochondrial and metabolic remodeling occur during myogenic differentiation

OPA1-mediated increase in SCAF1 is required for myogenic differentiation

Loss of OPA1 inhibits *in vivo* muscle regeneration and *in vitro* myogenesis

OPA1 regulates the metabolic switch that is essential for differentiation

Triolo et al., iScience 27, 109164
March 15, 2024
https://doi.org/10.1016/j.isci.2024.109164

iScience

CellPress
OPEN ACCESS

Article

Optic atrophy 1 mediates muscle differentiation by promoting a metabolic switch via the supercomplex assembly factor SCAF1

Matthew Triolo,[1] Nicole Baker,[1] Soniya Agarwal,[1] Nikita Larionov,[1] Tina Podinić,[1] and Mireille Khacho[1,2,*]

SUMMARY

Myogenic differentiation is integral for the regeneration of skeletal muscle following tissue damage. Though high-energy post-mitotic muscle relies predominantly on mitochondrial respiration, the importance of mitochondrial remodeling in enabling muscle differentiation and the players involved are not fully known. Here we show that the mitochondrial fusion protein OPA1 is essential for muscle differentiation. Our study demonstrates that OPA1 loss or inhibition, through genetic and pharmacological means, abolishes *in vivo* muscle regeneration and *in vitro* myotube formation. We show that both the inhibition and genetic deletion of OPA1 prevent the early onset metabolic switch required to drive myoblast differentiation. In addition, we observe an OPA1-dependent upregulation of the supercomplex assembly factor, SCAF1, at the onset of differentiation. Importantly, preventing the upregulation of SCAF1, through OPA1 loss or siRNA-mediated SCAF1 knockdown, impairs metabolic reprogramming and muscle differentiation. These findings reveal the integral role of OPA1 and mitochondrial reprogramming at the onset of myogenic differentiation.

INTRODUCTION

Skeletal muscle is a highly malleable tissue that requires remodeling in the face of changing metabolic and physical demands. Muscle mass is maintained in part through cycles of regeneration, whereby quiescent muscle stem cells (MuSCs) become activated in response to muscle damage. The resultant myoblasts proliferate to increase in number, and terminally differentiate and fuse into myofibers, in a process referred to as myogenesis. Although several intrinsic and extrinsic factors have been identified to mediate proper muscle regeneration,[1] in recent years mitochondrial reprogramming has been uncovered as a central regulator of this process,[2–5] yet the mechanisms have not been fully elucidated.

In general, lineage specific differentiation of committed stem cells is accompanied by a metabolic switch from glycolysis to mitochondrial respiration, through oxidative phosphorylation (OXPHOS), as the predominant source of energy generation.[6–8] Although this metabolic shift was once thought to be a means of upholding the higher metabolic demands of these differentiated cells, it is now clear that metabolic reprogramming is a regulatory mechanism that is essential for the process of differentiation.[6–9] For example, it is established that glycolytic proliferating myoblasts undergo a change in metabolic utilization whereby differentiated myotubes rely on mitochondrial OXPHOS for ATP generation.[10–15] The importance of this metabolic shift has been solidified in studies demonstrating that the inhibition of mitochondrial OXPHOS prevents appropriate muscle cell differentiation.[16–19] However, at present, it remains unclear how this metabolic switch is regulated.

Mitochondria are dynamic organelles that undergo cycles of fusion and fission in normal cell homeostasis and in cellular remodeling. Mitochondrial fission, the division of a mitochondrion, is largely regulated by the dynamic-related protein-1 (DRP1) in association with the endoplasmic reticulum and other mitochondrial fission factors (Mff, MiD49/51).[20] Conversely, mitochondrial fusion involves the tethering of the outer mitochondrial membrane, mediated by Mitofusin 1 and 2 (MFN1/2), and the inner mitochondrial membrane through optic atrophy 1 (OPA1).[20] Beyond its role in organelle fusion, OPA1 is integral to maintaining and adapting cristae architecture to moderate bioenergetic efficiency.[21–23] The importance of OPA1 is quite apparent in humans, whereby homozygous mutations in OPA1 lead to mtDNA depletion in skeletal muscle and loss of mitochondrial respiratory activity, resulting in neuromuscular weakness and fatality.[24] Furthermore, heterozygous mutations in OPA1 in humans lead to a condition referred to as dominant optical atrophy (DOA). Patients with DOA primarily suffer from loss of vision, but may also exhibit loss of hearing, peripheral neuropathy, and myopathy.[25]

Mitochondria and their dynamics have an established role in moderating skeletal muscle health across a lifespan.[26–28] Recently, we and others have begun to uncover the integral role of mitochondrial dynamics in the development of muscle, both *in vivo* and *in vitro*.[2–4,29–31] Seminal studies have demonstrated that OPA1 is required for the maintenance of muscle mass and function.[32,33] Importantly, a decrease

[1]Department of Biochemistry, Microbiology and Immunology, Center for Neuromuscular Disease (CNMD), Ottawa Institute of Systems Biology (OISB), Faculty of Medicine, University of Ottawa, Ottawa, ON K1H 8M5, Canada
[2]Lead contact
*Correspondence: mkhacho@uottawa.ca
https://doi.org/10.1016/j.isci.2024.109164

in OPA1 has been observed during aging in both muscle tissue and muscle stem cells.[3,32–34] The decline of OPA1 has many consequences for muscle homeostasis. First, decreased OPA1 in muscle tissue has been shown to cause muscle atrophy.[33] Furthermore, we recently found that the loss of OPA1 in MuSCs severely impacts their maintenance and self-renewal capacity.[3] However, the consequences of OPA1 loss on muscle regeneration capacity and differentiation potential have not been explored. Furthermore, given the important role of OPA1 in the regulation of mitochondrial function and bioenergetics, its role within the context of metabolic remodeling during the differentiation of muscle cells remains undefined. Thus, we hypothesize that OPA1 is required for muscle regeneration and the differentiation of myoblasts into myotubes by mediating the mitochondrial and associated metabolic remodeling that is necessary for myogenesis.

Using genetic and pharmacological targeting of OPA1 within *in vivo* and *in vitro* models, we have uncovered that OPA1 is essential for myogenic differentiation. First, we show that loss of OPA1 in MuSCs completely abolishes injury induced muscle regeneration. We uncover increases in the OPA1 expression and remodeling of mitochondrial structure and cristae architecture in the early phases of differentiation, favoring a greater contribution of mitochondrial energy production within these cells. Finally, we report that both inhibition and loss of OPA1 in muscle cells prevent the metabolic switch required for differentiation, in part through the downregulation of the mitochondrial super complex-related protein SCAF1.

RESULTS

Loss of OPA1 in muscle stem cells impairs *in vivo* muscle regeneration

Given the importance of OPA1 in muscle maintenance, we wanted to assess whether loss of OPA1 in muscle stem cells (MuSCs) would impact muscle regeneration. To do so, we used a tamoxifen-inducible knockout model of OPA1 in Pax7+ MuSCs (Opa1-Pax7CreERT2, referred to as OPA1-KO).[3] The tibialis anterior (TA) muscle of OPA1-WT and OPA1-KO mice was subjected to a cardiotoxin injury (CTX) injury model shortly after the last tamoxifen injection (3 days). Strikingly, loss of OPA1 completely abolished muscle regenerative capacity, with an apparent impairment visible as early as 4 days post-injury (DPI) (Figure 1A). H&E staining performed on cross-sections of TA muscle at 4, 7, and 21 DPI showed substantially decreased numbers of newly generated myofibers containing centrally located nuclei in early phases (4 and 7 DPI) and the later phase of muscle regeneration (21 DPI) (Figure 1B). Correspondingly, myofiber cross sectional area (CSA) of newly regenerated myofibers was also dramatically decreased in OPA1-KO mice at all time points (Figure 1C). This blunted regeneration resulted in 79% smaller TA mass at 21 DPI in OPA1-KO mice (Figures 1A and 1D) and indicated a potentially essential role for OPA1 in muscle regeneration.

We then assessed the levels of embryonic myosin heavy chain (eMHC) following CTX injury, which is typically expressed during the early stages of differentiation and turned off when myofibers have completed differentiation (Figure 1E). We observed sustained expression of eMHC in OPA1-KO muscle (Figures 1F–1H), which was corroborated by a lack of appropriate mature, adult, MHC isoforms in OPA1-KO muscle (Figure 1I). These data are suggestive of an impairment in the differentiation and maturation of muscle in OPA1-KO mice.

Since OPA1 is an essential player in mitochondrial dynamics, which can influence skeletal muscle metabolic phenotypes, we asked whether loss of OPA1 in MuSCs affects mitochondrial function in newly regenerated myofibers. To do so, we assessed cytochrome *c* oxidase (COX) and succinate dehydrogenase (SDH) activity in newly generated myofibers within the TA muscle of OPA1-WT and OPA1-KO mice at 21 DPI (Figure 1J). The majority of regenerated myofibers present in OPA1-KO TA muscle showed only low levels of staining for COX and SDH activity, compared to the intermediate and high levels observed in OPA1-WT controls (Figures 1K and 1L). Cumulatively, these data suggest that loss of OPA1 in MuSCs not only impairs the regeneration of myofibers, but those that do regenerate exhibit defective mitochondrial activity.

Inhibition of OPA1 function with MYLS22 prevents myoblast differentiation

Next, we wanted to confirm whether the loss in regenerative capacity in OPA1-KO mice is due to a failure to effectively differentiate. We utilized cultured myoblast cells, as a cell-autonomous model of muscle maturation, to examine the impact of OPA1 directly on myogenic differentiation in the absence of confounding effects on MuSC function or associated niche factors. Furthermore, a pharmacological approach using the OPA1 inhibitor MYLS22 was utilized.[35] In these experiments, both a "low" (25μM) and "high" (50μM) dose of this compound were used.[36,37] To ensure that these doses of MYLS22 effectively inhibited the mitochondrial fusion function of OPA1, myoblasts were treated with vehicle (DMSO), 25 or 50μM of MYLS22 for 48 h, and mitochondrial morphology was assessed using the immunofluorescence labeling of the outer-mitochondrial membrane protein Tom20 (Figure 2A). As expected, cells treated with MYLS22 had fragmented mitochondria compared to control cells, as observed by the presence of small punctate mitochondria at both low and high doses of MYLS22 (Figure 2A). Notably, these doses did not have detectable effects on cell viability (Figure S1).

To determine whether the inhibition of OPA1 function and the resultant mitochondrial fragmentation perturb myogenesis *in vitro*, we treated myoblast cells with MYLS22 at the onset of differentiation and monitored the formation of myotubes at 3, 5, and 7 days post-differentiation. Phalloidin staining (Figure 2B) and measurement of myotube fusion index (Figure 2C) revealed a striking time- and dose-dependent impairment in myotube formation in MYLSS22-treated cells compared to vehicle treated cells. Importantly, the inhibition of OPA1 prevented the formation of multinucleated myotubes from the onset of the myogenic differentiation process (3 days) and did not show any signs of progression toward differentiation even after 7 days (Figure 2B). Specifically, the lower 25μM dose of MYLS22 decreased the fusion index by 91%, 60%, and 88% at 3, 5, and 7 days, respectively (Figure 2C). Furthermore, the higher 50μM dose of MYLS22 completely prevented differentiation (Figure 2C). These data clearly show that the inhibition of OPA1 function impairs myogenic differentiation.

Next, we examined whether the inhibition of differentiation could be due to altered metabolic properties due to the inhibition of OPA1. In assessing global ATP levels, we failed to uncover any major ATP deficits in MYLS22-treated cells at 24, 72, or 120 h post-differentiation (Figure 2D), which represent the time points where MYLS22 effectively impaired myotube formation (Figures 2B and 2C). At 168-h

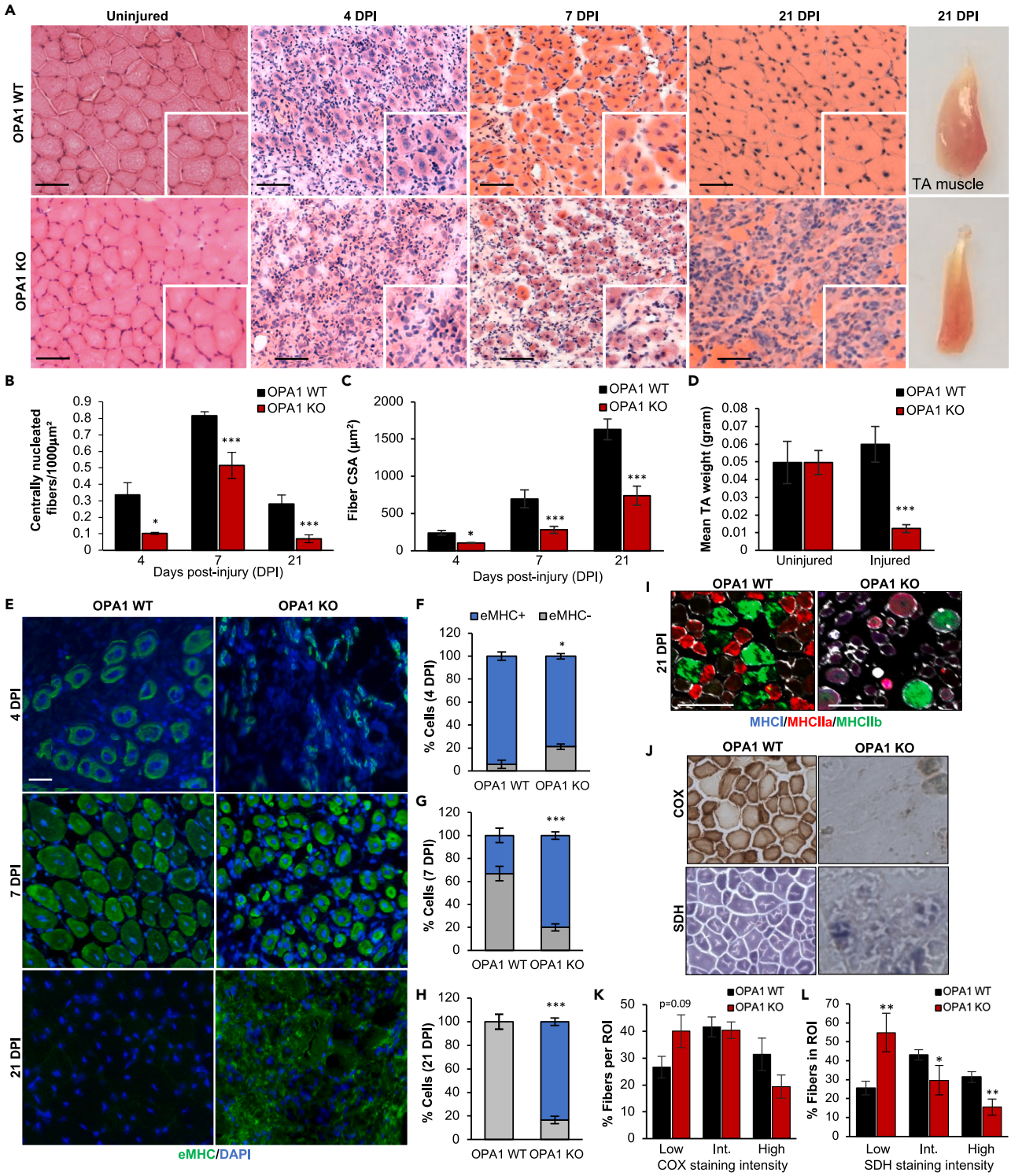

Figure 1. Loss of OPA1 in adult muscle stem cells impairs regenerative capacity following cardiotoxin injury

(A) Representative images of H&E-stained Tibialis Anterior (TA) muscle cross-sections from OPA1-WT and OPA1-KO uninjured muscle and following CTX-induced muscle regeneration at 4, 7 and 21 days post-injury (DPI). Visualization of the TA muscle at 21 DPI in OPA1-WT and OPA1-KO mice. Scale bars, 50 µM.

(B) Quantification of centrally nucleated myofibers at 4, 7 and 21 DPI. n ≥ 3 biological replicates, mean ± SD.

(C) Quantification of cross-sectional area of centrally nucleated myofibers following CTX injury at 4, 7 and 21 DPI. n ≥ 3 biological replicates, mean ± SD.

Figure 1. *Continued*

(D) Weight measurements of TA muscles from uninjured and following CTX injury at 21 DPI in OPA1-WT and OPA1-KO mice. n = 4 biological replicates, mean ± SD.

(E) Representative eMHC staining at 4, 7 and 21 DPI. Scale bar, 50 μM.

(F–H) Percent of myofibers that are eMHC positive (eMHC+) at (F) 4 DPI, (G) 7 DPI, and (H) 21 DPI. n = 4–7 ROI from 2 to 3 independent biological replicates., mean ± SEM.

(I) Representative muscle myofiber type staining from TA cross-sections at 21 DPI. Fiber boundaries are determined via Laminin (white). Scale bars, 100μm.

(J) Representative mitochondrial COX (top) and SDH (bottom) enzyme staining in TA cross-sections from OPA1-WT and OPA1-KO muscle following 21 DPI.

(K) COX staining intensity at 21 DPI in regenerated regions from OPA1-WT and OPA1-KO TA cross-sections. n = 3 ROI from 2 independent biological replicates, mean ± SEM.

(L) SDH staining intensity at 21DPI in regenerated regions from OPA1 WT and OPA1 KO TA cross-sections. n = 3 ROI from 2 independent biological replicates., mean ± SEM.

Statistics: (B-D, E-G, K&L): Unpaired t-test between OPA1 WT and OPA1 KO at each measured DPI. *p < 0.05, **p < 0.01, ***p < 0.001.

post-differentiation, there were, however, significant 22% and 92% deficits in ATP concentration in cells treated with 25 or 50μM of MYLS22, respectively (Figure 2D). Since the maintenance of global ATP levels in the presence of MYLS22 could be due to compensation from increased glycolysis, we examined the levels of ATP generated from mitochondrial-dependent versus non-mitochondrial means. As such, ATP levels were quantified in the presence of the ATP synthase inhibitor, oligomycin, to gain insight into the contribution of mitochondrial oxidative phosphorylation (OXPHOS) to global ATP levels (Figure 2E). Here, we report that MYLS22 treatment causes dose-dependent deficits in oligomycin-sensitive ATP levels (mitochondrial ATP generation) throughout the progression of differentiation (Figure 2E). These deficits were observed as early as 3-day post-differentiation with 50μM MYLS22 treatment (Figure 2E). To corroborate our ATP data, we utilized an *in vitro* oxygen consumption monitoring system and evaluated the oxygen consumption rate (OCR) during differentiation in cells incubated in the presence or absence of MYLS22. Analysis of OCR throughout the differentiation process revealed a significant dose effect of MYLS22 (Figures 2F and 2G), suggestive of mitochondrial impairments with OPA1 inhibition during differentiation. We further uncovered decrements in OCR as early as 6 h following the induction of differentiation in 50μM-treated cells, which was sustained throughout the full measurement period (Figures 2F and 2G). Importantly here, a sharp increase in OCR following 48 h of differentiation, likely representing a metabolic switch, was only observed in control cells and suggests that OPA1 function is required for metabolic reprogramming during differentiation.

To ensure these findings are not specific to the use of immortalized C2C12 murine muscle cells, we validated the results using primary muscle stem cells isolated from adult mouse skeletal muscle. Primary muscle cells were cultured and subjected to differentiation conditions in the presence or absence of 25μM MYLS22. Similar to C2C12 cells, differentiation of primary muscle cells was impaired by OPA1 inhibition (Figures 2H and 2I). Furthermore, monitoring OCR in primary muscle cells revealed an inability of cells treated with MYLS22 to increase oxygen consumption during differentiation (Figures 2J and 2K), as was observed in C2C12 cells. These results confirm an important role for OPA1 and mitochondrial remodeling at the onset of myogenic differentiation and for the proper formation of myotubes.

A metabolic switch occurs in the early phase of myogenic differentiation which is associated with mitochondrial remodeling and the upregulation of OPA1 and SCAF1

Given the striking effect of OPA1 loss on muscle differentiation, we wanted to dissect the OPA1 dependent functions during differentiation, including mitochondrial dynamics, cristae architecture, and bioenergetics. Since we observed that the major metabolic changes were occurring within the first 72 h of differentiation (Figure 2), we focused our subsequent analysis on the metabolic switch in this early differentiation period, which has not been previously assessed. First, we detected a time-dependent increase in OPA1 protein levels, but not OPA1 transcript levels, during early differentiation, which was significantly upregulated by ~4-fold as early as 48 h post-differentiation (Figures 3A and 3B). Using immunofluorescence, we uncovered a decrease in mean mitochondrial length at 24 h post-differentiation, followed by the presence of longer mitochondria by 72 h post-differentiation (Figures 3C–3E). This increase in mitochondrial length at 72 h post-differentiation was also observed using electron microscopy (Figures 3F and 3G).

Since cristae remodeling is largely impacted by OPA1, we also examined the dynamics in mitochondrial cristae architecture via TEM during the early stages of myogenesis (Figures 3F and 3H–3J). The mean number of cristae per mitochondria was increased in a time-dependent manner, significantly at 72 h (Figure 3H). Mean cristae width underwent an early increase (i.e., within the first 24-h period), followed by a decrease at 48 h (Figure 3I). Finally, mean cristae junction width was significantly reduced at 48 and 72 h post-differentiation (Figure 3J). Given that increased cristae biogenesis and cristae tightening are associated with enhanced mitochondrial function, this mitochondrial remodeling is suggestive of bioenergetic changes that occur during the differentiation of muscle cells.

The changes measured in mitochondrial architecture are typically associated with enhanced metabolic properties of these organelles. As such, we next examined global ATP levels and OCR during differentiation (Figures 3K–3M). We find that ATP levels are altered in a biphasic manner, such that they are increased in the early phase of post-differentiation (6 h) and then elevated again at 48 and 72 h (Figure 3K). At the level of the mitochondria, there were significant increases in OCR as early as 6 h post-differentiation, which continued to increase until it stabilized at 72 h (Figures 3L and 3M). Similarly, this time-dependent increase in OCR was evident in primary myoblasts (Figures S2B and S2C). These data indicate a metabolic reprograming within the first 72-h period of differentiation *in vitro*. Supportive of these metabolic changes, expression levels of electron transport chain (ETC) proteins, including components of Complex-1 (NDUFA9), Complex-II (SDHA), Complex-III (UQCRC2), Complex-IV (MTCO1), and Complex-V (ATP5a), were increased during differentiation (Figure 3N). Given the rapid

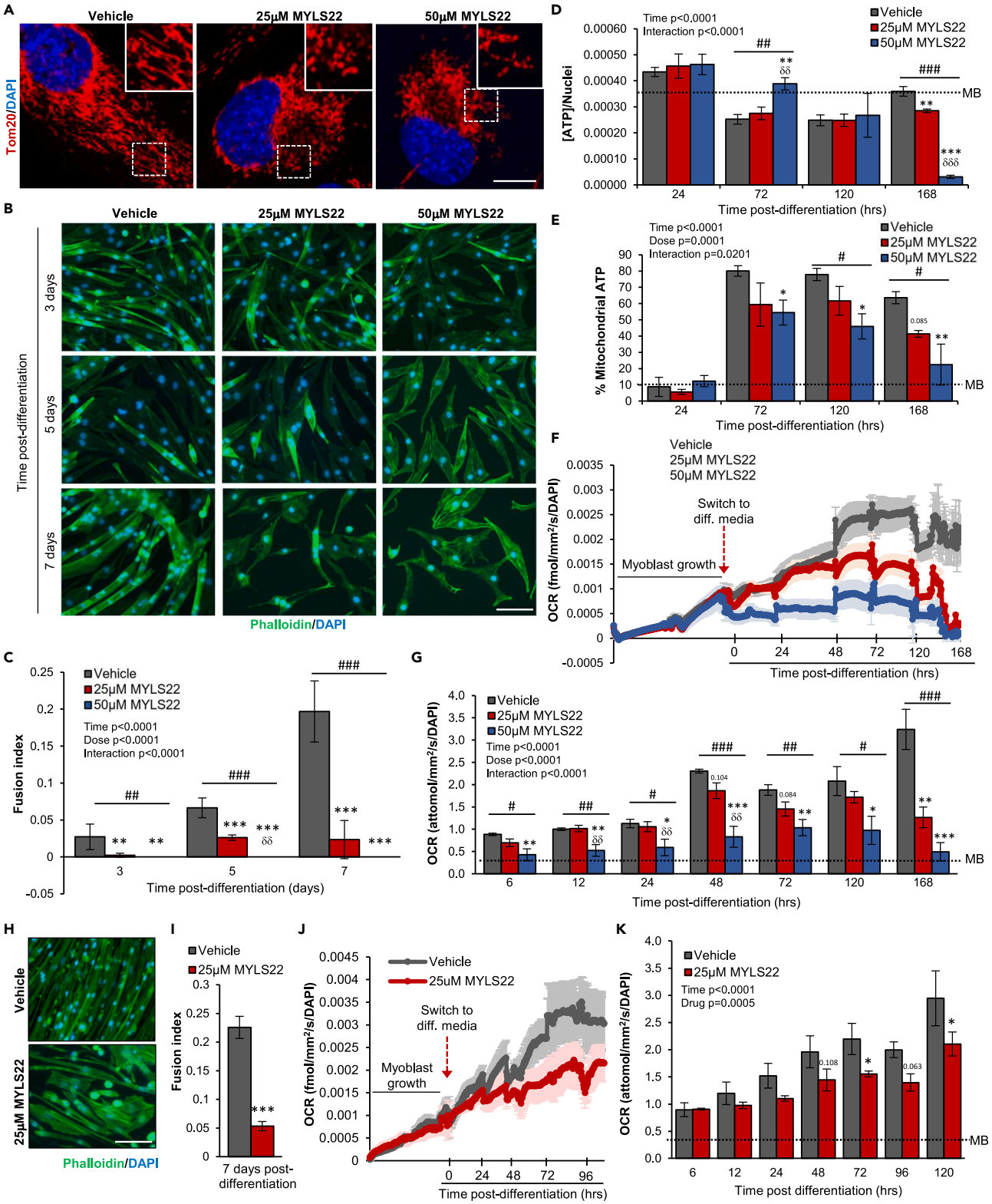

Figure 2. Inhibition of OPA1 with MYLS22 impairs differentiation and suppresses mitochondrial energy generation

(A) Representative immunofluorescence images of mitochondria (Tom20) in Vehicle (DMSO) treated myoblasts (MBs) and following 48 h of treatment with 25 μM or 50 μM MYLS22. Insets are zoomed views of dotted boxes. Scale bar, 10 μM.

Figure 2. *Continued*

(B) Representative images of Phalloidin (green) and DAPI (blue) staining in differentiating myoblast cells treated with Vehicle, 25 μM or 50 μM MYLS22 at 3, 5 and 7 days post-differentiation. Scale bar, 100 μM.

(C) Quantification of myotube fusion index (i.e., cells containing ≥3 nuclei) in myoblast cells treated with Vehicle, 25 μM or 50 μM MYLS22 at 3, 5 and 7 days post differentiation. n ≥ 3, mean ± SD.

(D) ATP levels in differentiating myoblast cells treated with Vehicle, 25 μM or 50 μM MYLS22 for 24, 72, 120 and 168 h post-differentiation. ATP levels for myoblasts (MBs) is represented by the dashed line. n = 3 independent experiments, each with 3 technical replicates, mean ± SEM.

(E) Graph indicates ATP levels following 30 min oligomycin treatment represented as percent mitochondrial ATP (oligomycin-sensitive ATP generated by OXPHOS) relative to the total ATP in the cell. Myoblast cells treated with Vehicle, 25 μM MYLS22 or 50 μM MYLS22 for 24, 72, 120 or 168 h. Myoblasts (MBs) are represented by the dashed line. n ≥ 3 independent experiments, each with 3 technical replicates, mean ± SEM.

(F) Tracing of live cell-respirometry oxygen consumption rate (OCR) during periods of myoblast growth and differentiation in myoblast cells treated with Vehicle, 25 μM MYLS22 or 50 μM MYLS22. Traces represent the mean of 4 independent experiments, and light shading represents ±SEM of 4 biological replicates.

(G) Quantification of OCR in myoblasts (MBs) and during the differentiation of cells treated with Vehicle, 25 μM MYLS22 or 50 μM MYLS22. Myoblasts (MBs) are represented by the dashed line. N = 4 independent experiments, mean ± SEM.

(H) Representative images of Phalloidin (green) and DAPI (blue) staining in 7 days differentiated primary myoblast cells treated with Vehicle or 25 μM MYLS22. Scale bar, 100 μM.

(I) Quantification of myotube fusion index (i.e., cells containing ≥3 nuclei) in primary myoblast cells treated with Vehicle or 25 μM MYLS22 at 7 days post differentiation. n ≥ 3, mean ± SEM.

(J) Tracing of live cell-respirometry oxygen consumption rate (OCR) during periods of primary myoblast proliferation and differentiation treated with Vehicle or 25 μM MYLS22. Trace represents the mean of 3 experiments, and light gray represents ±SEM.

(K) Quantification of OCR in primary myoblasts (MBs) and during differentiation in the presence of Vehicle or 25 μM MYLS22. Primary myoblasts (MBs) are represented by the dashed line. n = 3 independent experiments, mean ± SEM.

Statistics: (C, D, E, G) Two-Way ANOVA to evaluate the main effect of time of differentiation, the main effect of MYLS22 drug dose and the interaction between the two variables; significant changes are indicated in text. (C, D, E, G) One Way ANOVA to evaluate the effect of drug dose within each given time point; #$p < 0.05$, ##$p < 0.01$, ###$p < 0.001$. Fischer LSD post-hoc test to assess individual differences between data points; *$p < 0.05$, **$p < 0.01$, ***$p < 0.001$ to represent differences between Veh and MYLS22 and δ $p < 0.05$, δδ $p < 0.01$, δδδ $p < 0.001$ to represent differences between 25 μM and 50 μM of MYLS22. (E) Unpaired t-test to evaluate the effect of 50 μM compared to Veh. *$p < 0.05$. (I) Unpaired t-test to evaluate the effect of 25 μM compared to Veh; **$p < 0.01$. (K) Two-Way ANOVA to evaluate the main effect of time of differentiation, the main effect of 25 μM MYLS22 and the interaction between the two variables; significant changes are indicated in text. Fischer LSD post-hoc rest to assess individual differences *$p < 0.05$ at indicated time points.

See also Figure S1.

increase in mitochondrial respiration observed during the early stage of differentiation, we sought to investigate the expression of the supercomplex assembly factor SCAF1 (also known as Cox7a2l), which is a master regulator of mitochondrial supercomplex formation and mitochondrial respiratory efficiency.[38–40] Surprisingly, there was a rapid and time-dependent increase in the protein levels of SCAF1 during differentiation (Figures 3O and 3P), as well as an increase in SCAF1 gene expression (Figure 3Q). In corroboration with increased SCAF1 protein levels observed via immunoblotting, we also detected a greater abundance and mitochondrial localization of SCAF1 using immunofluorescence (Figures 3R and 3S). These data suggest both the structural and functional remodeling of mitochondria during the early phases of myoblast differentiation into myotubes. Furthermore, this represents the first observation of a possible developmental role for SCAF1 during differentiation.

Decreased expression of OPA1 and SCAF1 prevent mitochondrial reprogramming and impairs myogenic differentiation

To investigate any potential relationship between OPA1 and SCAF1, an siRNA-mediated approach was used to decrease the expression of either protein in myoblasts. Effective siRNA-targeted knockdown of OPA1 or SCAF1 was validated by both protein and gene expression (Figures 4A–4D). Unexpectedly, we found that the knockdown of OPA1 resulted in decreased SCAF1 mRNA and protein expression (Figures 4C–4E). Meanwhile, the knockdown of SCAF1 did not have any detectable effects on OPA1 expression (Figures 4A and 4E). As follows, mitochondrial length was reduced in siOPA1 myoblasts and maintained a fragmented phenotype even after 3 days of differentiation (Figures 4F and 4G). In contrast, mitochondrial length was not affected in cells lacking SCAF1 (Figures 4F and 4G). These data suggest that OPA1 is required for the expression of SCAF1 in myoblasts and may act as an upstream regulator of SCAF1 during differentiation.

To evaluate if the metabolic profile of proliferating or differentiating myoblasts is similarly influenced by siOPA1 or siSCAF1, we measured ATP levels in cells treated with or without oligomycin for 30 min to assess global versus mitochondrial-dependent ATP levels (Figure 4H). In proliferating myoblasts, which rely mostly on glycolysis for ATP generation, no detectable differences were observed in siOPA1 or siSCAF1 cells following oligomycin treatment (Figure 4H left). Following 3 days post-differentiation, control cells show an approximate 60% drop in ATP levels following the inhibition of OXPHOS with oligomycin indicating that these cells have now altered their metabolic reliance on OXPHOS as a major source of ATP generation (Figure 4H, right). However, at 3 days post-differentiation both siOPA1 and siSCAF1 cells did not exhibit a drop in ATP levels with oligomycin treatment that is comparable to controls (Figure 4H, right). This manifested in significant reductions in mitochondrial ATP levels (Figure 4I) in both knockdown models, suggestive of impaired mitochondrial OXPHOS in the absence of OPA1 or SCAF1. Cumulatively, these data indicate that siOPA1 and siSCAF1 cells failed to undergo a metabolic switch toward a predominant reliance on OXPHOS during differentiation. Finally, to determine if loss of OPA1 or SCAF1 ultimately impact myogenic differentiation, we measured the myotube fusion index at 7 days post-differentiation (Figures 4J and 4K). We found that knockdown of OPA1 or SCAF1 caused a profound impairment in myoblast differentiation (Figures 4J and 4K). These data show that OPA1-mediated mitochondrial remodeling and metabolic reprogramming, in part through SCAF1, are essential for myogenic differentiation.

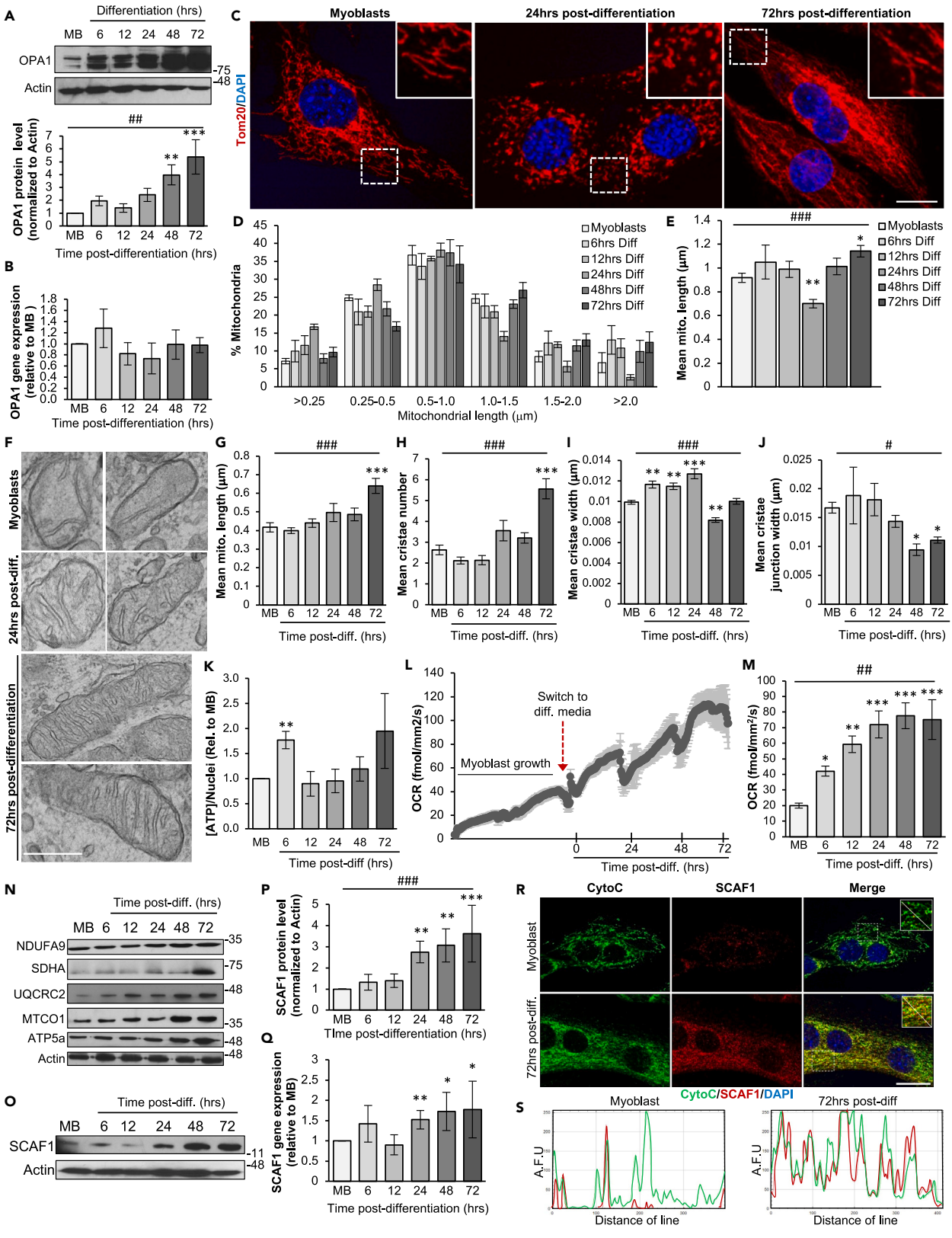
A
Differentiation (hrs)
MB 6 12 24 48 72
OPA1
Actin
-75
-48
##
***
**
OPA1 protein level (normalized to Actin)
Time post-differentiation (hrs)
B
OPA1 gene expression (relative to MB)
Time post-differentiation (hrs)
C
Myoblasts
24hrs post-differentiation
72hrs post-differentiation
Tom20/DAPI
D
% Mitochondria
Myoblasts
6hrs Diff
12hrs Diff
24hrs Diff
48hrs Diff
72hrs Diff
>0.25
0.25-0.5
0.5-1.0
1.0-1.5
1.5-2.0
>2.0
Mitochondrial length (μm)
E
###
Mean mito. length (μm)
F
Myoblasts
24hrs post-diff.
72hrs post-differentiation
G
###
Mean mito. length (μm)
Time post-diff. (hrs)
H
###
Mean cristae number
I
###
Mean cristae width (μm)
J
#
Mean cristae junction width (μm)
K
[ATP]/Nuclei (Rel. to MB)
L
Switch to diff. media
Myoblast growth
OCR (fmol/mm2/s)
M
##
N
NDUFA9
SDHA
UQCRC2
MTCO1
ATP5a
Actin
O
SCAF1
P
SCAF1 protein level (normalized to Actin)
Q
SCAF1 gene expression (relative to MB)
R
CytoC
SCAF1
Merge
CytoC/SCAF1/DAPI
S
A.F.U
Distance of line

Figure 3. Differentiation of muscle cells is characterized by an increase in OPA1 protein, mitochondrial remodeling, a metabolic switch favoring OXPHOS and increased SCAF1 expression

(A) Representative western blot and quantification of OPA1 protein in myoblasts (MB) and during the differentiation of myoblast cells. Data normalized to MB from within the same experiment. OPA1 n ≥ 6, mean ± SEM.

(B) OPA1 gene expression during the differentiation of myoblast cells. n ≥ 4 independent experiments, mean ± SEM.

(C) Representative immunofluorescence images of mitochondria (Tom20) in myoblasts and at 24 and 72 h following the onset of differentiation. Insets are zoomed views of dotted boxes. Scale bar, 5 μM.

(D) Mitochondrial length distribution in myoblasts or during differentiation at the indicated time points. n > 500 mitochondria per condition, mean ± SEM.

(E) Mean mitochondrial length in myoblasts or following the induction of differentiation in myoblast cells. n > 500 mitochondria per time point, mean ± SEM.

(F) Representative EM images of mitochondrial ultrastructure in myoblasts, and at 24, 48 and 72 h post-differentiation. Scale bar, 0.25 μM.

(G) Quantification of mitochondrial length from EM analysis. n ≥ 45 mitochondria per indicated time point, mean ± SEM.

(H) Quantification of number of cristae per mitochondria from EM analysis. n ≥ 45 mitochondria per indicated time point, mean ± SEM.

(I) Quantification of mean cristae width per mitochondria from EM analysis. n ≥ 155 cristae per indicated time point, mean ± SEM.

(J) Quantification of mean cristae junction width per mitochondria from EM analysis. n ≥ 36 cristae junctions per indicated time point, mean ± SEM.

(K) ATP levels in myoblasts (MBs) and during differentiation. n = 3 independent experiments each with three replicates, mean ± SEM.

(L) Tracing of live cell-respirometry oxygen consumption rate (OCR) during periods of myoblast growth and differentiation. Trace represents the mean of 3 experiments, and light gray represents ±SEM.

(M) Quantification of OCR in myoblasts (MBs) and during differentiation. n = 3 independent experiments., mean ± SEM.

(N) Representative western blot of the mitochondrial electron transport chain proteins NDUFA9 (Complex I), SDHA (Complex II), UQCRC2 (Complex III), MTCO1 (CIV), and ATP5a (Complex V) in MBs and during differentiation.

(O) Representative western blot of SCAF1 protein in myoblasts and during differentiation.

(P) Quantification of SCAF1 protein in myoblasts and during differentiation. Data is normalized to myoblasts from within the same experiment. n = 4, mean ± SEM.

(Q) SCAF1 gene expression during myoblast differentiation. n = 7 independent experiments, mean ± SEM.

(R) Representative immunofluorescence images of mitochondria (Cytochrome *c*, green) and SCAF1 (red). Yellow color in merged image indicates the co-localization of SCAF1 to mitochondria. Insets are zoomed views of dotted boxes. Scale bars, 20 μM.

(S) Representative co-localization analysis of zoom inset image from (R).

Statistics: (A, B, E, G-K, M, P, Q) One Way ANOVA to evaluate the effect of time during differentiation; #p < 0.05, ##p < 0.01, ###p < 0.001. Fischer LSD post-hoc test to assess individual differences between MB and time points after the onset of differentiation; *p < 0.05, **p < 0.01, ***p < 0.001.

See also Figure S2.

DISCUSSION

Myogenic differentiation, the transition from myoblast to myotube, is integral for skeletal muscle tissue repair. There is a well-documented metabolic switch associated with the differentiation of myoblasts into myotubes,[19,41] which is accompanied by changes in mitochondrial morphology that favors network formation in myotubes.[42] Furthermore, although the essential role for mitochondrial dynamics in the maintenance of cell homeostasis is established, the importance of the mitochondrial fusion protein, OPA1, and its role in fusion and mitochondrial membrane remodeling during myogenesis remains elusive. In the present study, we aimed to address the hypothesis that OPA1 is required for organellar remodeling necessary with myogenic differentiation. We demonstrate that genetic loss of OPA1 impairs *in vivo* muscle regeneration following injury. Using myoblast cell culture models of *in vitro* differentiation, the present work uncovered that the genetic and pharmacological inhibition of OPA1 impaired myotube formation, which coincided with a failure to effectively undergo a metabolic switch from glycolytic to mitochondrial metabolism. We further uncovered that OPA1 regulates the levels of mitochondrial supercomplex assembly factor, SCAF1, which is integral for the progression of myogenic differentiation. These findings provide essential evidence into the contribution of OPA1 in the regulation of the metabolic switch required for cellular differentiation.

To understand how OPA1 may be regulating the differentiation of myoblasts into myotubes, we characterized the mitochondrial phenotype in the early phase (i.e., first 72 h) of myotube formation, as this is a period in which we observed metabolic remodeling of differentiating cells. First, mitochondrial length and cristae number are increased at the 48- and 72-h periods, suggesting that mitochondrial fusion events take place. Focusing on cristae architecture, increases in their width and junction width are typically associated with reduced metabolic capacity, increased ROS production, mitochondrial fission, and mitochondrial-mediated apoptosis.[43,44] Thus, the initial increase in mitochondrial cristae width that we measured may pre-dispose these organelles to produce ROS as a mechanism to signal toward fission and mitophagy, which has been shown to occur in this period.[42,45–47] Conversely, cristae width and junction compaction are associated with metabolic efficiency.[43,44] As such, the subsequent decrease in mean cristae width, coupled with the decrease in mitochondrial cristae junction width that was measured at 48 and 72 h post-differentiation are suggestive of enhanced ETC functionality. In fact, by monitoring oxygen consumption in live cells during differentiation, we were able to uncover this metabolic shift, favoring mitochondrial energy production.

Cristae architecture and mitochondrial metabolic efficiency are largely controlled by OPA1.[43,44] Thus, based on our findings, the measured increase in OPA1 protein that we and others,[42] report during differentiation serves as a mechanism for mitochondrial remodeling to favor enhanced mitochondrial metabolism in myotubes. Although previous studies have interrogated how the loss or inhibition of other mitochondrial fusion and fission factors influence *in vitro* myogenesis,[2,30] no studies have yet evaluated whether OPA1 is required for myogenic differentiation. As such, we are the first to report that both genetic knockdown and pharmacologic inhibition of OPA1 during muscle differentiation prevent the formation of myotubes. Thus, it is likely that the failed regeneration that we observed following *in vivo* cardiotoxin injury in

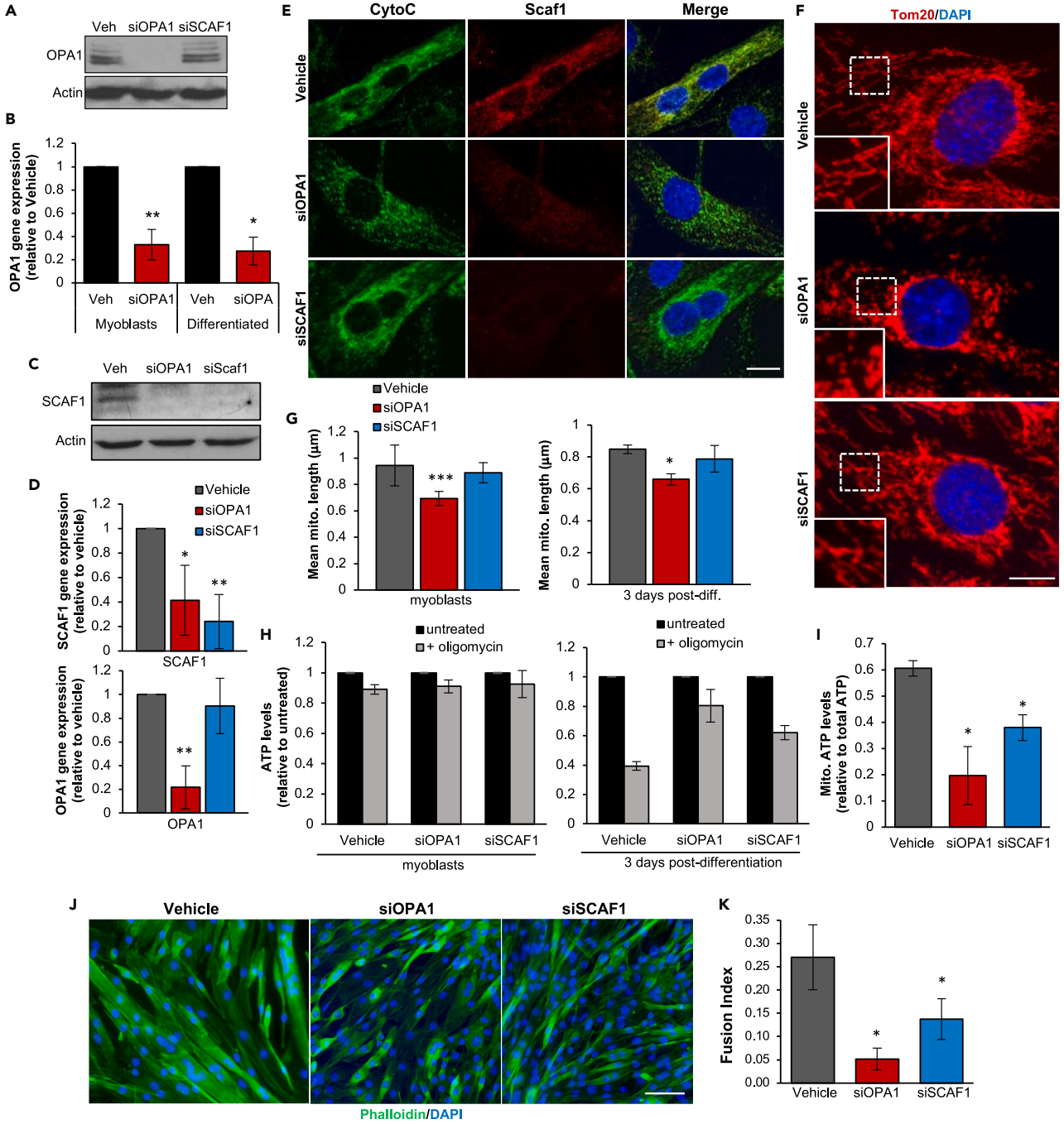

Figure 4. Deletion of OPA1 or SCAF1 prevents the metabolic switch to OXPHOS and inhibits muscle differentiation

(A) Representative western blot of OPA1 protein in untreated myoblasts (MB) or those treated with Vehicle, siOPA1 or siSCAF1.

(B) OPA1 gene expression in myoblasts and in 3-day differentiated myoblast cells. n = 2–3 independent experiments, mean ± SEM.

(C) Representative western blot for SCAF1 in myoblasts treated with vehicle or siRNA targeting OPA1 or SCAF1.

(D) SCAF1 and OPA1 gene expression in myoblasts treated with Vehicle, or siRNA targeting OPA1 and SCAF1. n = 3 independent experiments, mean ± SD.

(E) Representative immunofluorescence images of mitochondria (Cytochrome *c*, green) and SCAF1 (red) in Vehicle, siOPA1 or siSCAF1 treated cells that were differentiated for 3 days. Yellow color in merged image indicates the co-localization of SCAF1 to mitochondria. Scale bar, 5 µM.

(F) Representative immunofluorescence images of mitochondria (Tom20) in Vehicle, siOPA1 and siSCAF1 myoblasts. Insets are zoomed views of dotted boxes. Scale bar, 10 µM.

(G) Mean mitochondrial length in Vehicle, siOPA1 or siSCAF1 treated myoblasts (left) or following 3 days of differentiation (right). n ≥ 300–500 mitochondria per time point, mean ± SD.

Figure 4. *Continued*

(H) ATP levels at steady state (black bars) and after 30min of oligomycin treatment (gray bars) in Vehicle, siOPA1 and siSCAF1 myoblasts (left) and following 3 days of differentiation(right). n = 3 independent experiments, each with 3 technical replicates, mean ± SD.

(I) Relative mitochondrial generated ATP (oligomycin-sensitive ATP) in Vehicle, siOPA1 and siSCAF1 following 3 days of differentiation. n = 3 independent experiments, each with 3 technical replicates, mean ± SD.

(J) Representative immunofluorescence images of Phalloidin (green) and DAPI (blue) in Vehicle, siOPA1, and siSCAF1 at 7 days post-differentiation. Scale bar, 50 μM.

(K) Quantification of myotube fusion index (i.e., cells containing ≥3 nuclei) at 7 days post-differentiation in Vehicle, siOPA1 and siSCAF1 cells. n = 3 biological replicates., mean ± SEM.

Statistics: (A-D, G-I, K) Unpaired t-test Vehicle (Lipofectamine) vs. siRNA treated cells; *p < 0.05, **p < 0.01, ***p < 0.001.

OPA1-KO mice is due to failed muscle maturation. This interpretation is supported by the sustained eMHC staining of regenerating fibers, and the lack of mature MHC isoform expression.

To assess why the loss of OPA1 completely abolished the generation of myotubes, we focused on the role of OPA1 in mediating mitochondrial metabolic function. Utilizing a novel OPA1 inhibitor, MYLS22,[35] we investigated the role of OPA1 function in the regulation of the metabolic switch as myoblasts transition to myotubes. Surprisingly, we did not detect substantial changes in global ATP during the early phases of myogenesis. However, since impairments in mitochondrial ATP generation were present, it may be that non-mitochondrial sources of ATP compensated in MYLS22 treated cells. Interestingly, live-cell respiration of MYLS22-treated C2C12 cells uncovered dose-dependent decrements in OCR throughout the course of differentiation (i.e., from 6 h through to 7 days post differentiation), indicating that functional OPA1 is necessary for the required increase in mitochondrial metabolism during the differentiation process. As C2C12 cells may not accurately reflect the myogenesis of primary cells, we further corroborated these data in myoblasts derived from murine muscle. This would indicate a conserved mechanism, by which OPA1 regulates the differentiation of muscle through the control of mitochondrial metabolic plasticity. We also show that siRNA knockdown of OPA1 also prevents this metabolic switch and myotube formation.

Finally, we also examined whether the supercomplex assembly factor, SCAF1, is differentially expressed in myoblasts and developing myotubes. Previous studies have extensively investigated the importance of SCAF1 in mitochondrial function associated with cellular adaptations to stress.[48–51] Thus, we were surprised to find that both SCAF1 mRNA and protein are upregulated during the differentiation process. This is the first time, to our knowledge, that SCAF1 has been investigated in the context of a physiologic developmental process. As OPA1 is required for cristae architectural remodeling and the metabolic switch during muscle cell differentiation, we questioned whether it may also be necessary for proper ETC assembly. Thus, we evaluated SCAF1 gene expression and protein in siOPA1 myoblasts and found that loss of OPA1 reduced SCAF1 expression. Finally, by knocking down SCAF1, we were able to identify the fundamental role of this protein in the regulation of the metabolic switch with differentiation. Cumulatively, these lines of evidence indicate that OPA1 is required for myogenic differentiation through its ability to moderate mitochondrial structure, cristae architecture, and metabolic efficiency, in part, mediated by SCAF1.

Other mitochondrial dynamics machinery have been shown to change during myogenic differentiation. This includes 1) an increase in the content[30,42] and mitochondrial localization[30,47] of the fission factor DRP1 early in the differentiation program of muscle cells, and 2) an upregulation of MFN2 as early as 1-day post-differentiation induction.[2] Importantly, the inhibition of DRP1 with Mdivi-1 prevents myogenic differentiation,[30,47] alike what is observed in our present study with inhibition and knockdown of OPA1. In contrast to our present data indicating that OPA1 is required for the metabolic remodeling of muscle cells, DRP1 inhibition induces cell death signaling to stop differentiation.[30,47] It is plausible that DRP1 is required for the provision of mitochondria through the mitophagy system, and with insufficient fission, cell death-signaling ensues. Supportively, mitophagy is required for *in vitro* myogenesis.[42,52] In contrast, MFN2 is dispensable for muscle regeneration and myogenesis.[2] Cumulatively, these data provide evidence that dynamics proteins have functionally distinct roles in the remodeling of mitochondria that is required for myogenic differentiation. Further, this solidifies the importance of OPA1 in the metabolic reprograming of differentiating muscle cells, likely through the ability to dictate inner mitochondrial membrane architecture and supercomplex formation via SCAF1.

The findings from the present, preclinical, study have vast implications for the pathophysiology of skeletal muscle. For example, individuals with heterozygous OPA1 mutations display severe muscle myopathy.[53,54] Myopathy in these individuals is typically associated with impairments confined within the muscle fiber. However, based on the results of the present study, it is plausible that the deterioration of the muscle is further contributed by impaired muscle regeneration. Furthermore, since early post-natal skeletal muscle development is characterized by the fusion of muscle progenitor cells to increase myonuclear number and muscle growth,[55] it is likely that these patients have perturbed post-natal muscle development. In addition, during aging and denervation induced muscle atrophy, skeletal muscle OPA1 levels are substantially reduced.[33,56] Furthermore, we have previously reported that OPA1 is downregulated in aging MuSCs.[3] Thus, it is plausible that the loss of OPA1 during aging and atrophy contributes to a deterioration of muscle through defects in regenerative capacity via a failure of myogenic progenitors to terminally differentiate. Promisingly, overexpression of OPA1 has been found to enhance skeletal muscle and MuSC function during aging.[3,56] Thus, our findings, in corroboration with these discoveries, provide optimism that interventions aimed at enhancing OPA1 function may augment regenerative capacity through sustained myogenic differentiation.

Limitations of the study

The OPA1-KO mice utilized in the present study are under the control of the Pax7 promoter,[3] implying that OPA1 expression is only perturbed in MuSCs. Thus, the ablation of regenerative capacity following injury may be caused by failure of other myogenic processes prior to differentiation, as we have previously reported.[3] Furthermore, in the present study, we genetically ablate OPA1 levels or inhibit its function

pharmacologically. However, it is appreciated that OPA1 isoforms exist, including the long (L-OPA1) and short (S-OPA1), and undergo complex processing to moderate inner mitochondrial membrane fusion and cristae architecture.[57–59] Thus, although this study uncovers the overall importance of OPA1, the involvement of isoforms, if any, remains undefined. Furthermore, the question of whether OPA1 processing regulates the differentiation of skeletal muscle cells presents as a promising avenue of future study.

STAR★METHODS

Detailed methods are provided in the online version of this paper and include the following:

- KEY RESOURCES TABLE
- RESOURCE AVAILABILITY
  - Lead contact
  - Materials availability
  - Data and code availability
- EXPERIMENTAL MODEL AND STUDY PARTICIPANT DETAILS
  - Mouse models
  - Cell lines
- METHOD DETAILS
  - Cardiotoxin injury
  - Muscle fixation and sectioning
  - Hematoxylin and Eosin staining and quantification of muscle regeneration
  - eMHC staining and quantification of muscle regeneration
  - Muscle fiber type staining
  - Cytochrome C xidase (COX) and succinate dehydrogenase (SDH) staining
  - siRNA-mediated knockdown of OPA1 and SCAF1
  - Inhibition of OPA1 with MYLS22
  - Immunofluorescence staining
  - Electron microscopy of myoblasts and differentiating myotubes
  - ATP measurements
  - Assessing cellular respiration *in vitro*
  - RNA extraction and qPCR
  - Protein analysis by western blot
- QUANTIFICATION AND STATISTICAL ANALYSIS

SUPPLEMENTAL INFORMATION

Supplemental information can be found online at https://doi.org/10.1016/j.isci.2024.109164.

ACKNOWLEDGMENTS

This work was supported by funds from Canada Research Chair (CRC), CIHR, Stem Cell Network, NSERC and J.P. Bickell to M.K. M.T has been supported by a Muscular Dystrophy Canada Research Fellowship in collaboration with the Neuromuscular Disease Network for Canada. We thank the University of Ottawa Cell Biology and Image Acquisition Core Facility (CBIA RRID (SCR_021845), the University of Ottawa Electron Microscopy Core Facility, the University of Ottawa Louis Pelletier Histology Core Facility, and the Facility for Electron Microscopy Research at McGill University.

AUTHOR CONTRIBUTIONS

M.K. conceptualized and led the study. M.K., N.B., M.T., and S.A. designed and performed the experiments, and quantified data. T.P. performed the eMHC analysis in Figure 1 and initial SCAF1 gene expression experiments. N.L. performed Tamoxifen gavage, Cardiotoxin injections, animal colony maintenance, and muscle tissue sectioning. M.T. and M.K. wrote the article and designed the figures.

DECLARATION OF INTERESTS

The authors declare no competing interests.

Received: August 25, 2023
Revised: December 8, 2023
Accepted: February 5, 2024
Published: February 9, 2024

REFERENCES

1. Relaix, F., Bencze, M., Borok, M.J., Der Vartanian, A., Gattazzo, F., Mademtzoglou, D., Perez-Diaz, S., Prola, A., Reyes-Fernandez, P.C., Rotini, A., and Taglietti. (2021). Perspectives on skeletal muscle stem cells. Nat. Commun. *12*, 692. https://doi.org/10.1038/s41467-020-20760-6.
2. Luo, N., Yue, F., Jia, Z., Chen, J., Deng, Q., Zhao, Y., and Kuang, S. (2021). Reduced electron transport chain complex I protein abundance and function in Mfn2-deficient myogenic progenitors lead to oxidative stress and mitochondria swelling. Faseb. J. *35*, e21426. https://doi.org/10.1096/fj.202002464R.
3. Baker, N., Wade, S., Triolo, M., Girgis, J., Chwastek, D., Larrigan, S., Feige, P., Fujita, R., Crist, C., Rudnicki, M.A., et al. (2022). The mitochondrial protein OPA1 regulates the quiescent state of adult muscle stem cells. Cell Stem Cell *29*, 1315–1332.e9. https://doi.org/10.1016/j.stem.2022.07.010.
4. Hong, X., Isern, J., Campanario, S., Perdiguero, E., Ramírez-Pardo, I., Segalés, J., Hernansanz-Agustín, P., Curtabbi, A., Deryagin, O., Pollán, A., et al. (2022). Mitochondrial dynamics maintain muscle stem cell regenerative competence throughout adult life by regulating metabolism and mitophagy. Cell Stem Cell *29*, 1506–1508. https://doi.org/10.1016/j.stem.2022.09.002.
5. Yucel, N., Wang, Y.X., Mai, T., Porpiglia, E., Lund, P.J., Markov, G., Garcia, B.A., Bendall, S.C., Angelo, M., and Blau, H.M. (2019). Glucose Metabolism Drives Histone Acetylation Landscape Transitions that Dictate Muscle Stem Cell Function. Cell Rep. *27*, 3939–3955.e6. https://doi.org/10.1016/j.celrep.2019.05.092.
6. Mandal, S., Lindgren, A.G., Srivastava, A.S., Clark, A.T., and Banerjee, U. (2011). Mitochondrial function controls proliferation and early differentiation potential of embryonic stem cells. Stem Cell. *29*, 486–495. https://doi.org/10.1002/stem.590.
7. Shyh-Chang, N., Daley, G.Q., and Cantley, L.C. (2013). Stem cell metabolism in tissue development and aging. Development *140*, 2535–2547. https://doi.org/10.1242/dev.091777.
8. Takubo, K., Nagamatsu, G., Kobayashi, C.I., Nakamura-Ishizu, A., Kobayashi, H., Ikeda, E., Goda, N., Rahimi, Y., Johnson, R.S., Soga, T., et al. (2013). Regulation of glycolysis by Pdk functions as a metabolic checkpoint for cell cycle quiescence in hematopoietic stem cells. Cell Stem Cell *12*, 49–61. https://doi.org/10.1016/j.stem.2012.10.011.
9. Ryall, J.G., Dell'Orso, S., Derfoul, A., Juan, A., Zare, H., Feng, X., Clermont, D., Koulnis, M., Gutierrez-Cruz, G., Fulco, M., and Sartorelli, V. (2015). The NAD(+)-dependent SIRT1 deacetylase translates a metabolic switch into regulatory epigenetics in skeletal muscle stem cells. Cell Stem Cell *16*, 171–183. https://doi.org/10.1016/j.stem.2014.12.004.
10. Lyons, C.N., Leary, S.C., and Moyes, C.D. (2004). Bioenergetic remodeling during cellular differentiation: changes in cytochrome c oxidase regulation do not affect the metabolic phenotype. Biochem. Cell. Biol. *82*, 391–399. https://doi.org/10.1139/o04-040.
11. Leary, S.C., Battersby, B.J., Hansford, R.G., and Moyes, C.D. (1998). Interactions between bioenergetics and mitochondrial biogenesis. Biochim. Biophys. Acta *1365*, 522–530. https://doi.org/10.1016/s0005-2728(98)00105-4.
12. Elkalaf, M., Anděl, M., and Trnka, J. (2013). Low glucose but not galactose enhances oxidative mitochondrial metabolism in C2C12 myoblasts and myotubes. PLoS One *8*, e70772. https://doi.org/10.1371/journal.pone.0070772.
13. Yucel, N., Wang, Y., Mai, T., Porpiglia, E., Lund, P.J., Markov, G., Garcia, B.A., Bendall, S.C., Angelo, M., and Blau, H.M. (2019). Glucose metabolism drives histone acetylation landscape transitions that dictate muscle stem cell function. Cell Rep. *27*, 3939–3955. https://doi.org/10.1016/j.celrep.2019.05.092.
14. Hoffmann, C., Höckele, S., Kappler, L., Hrabě de Angelis, M., Häring, H., and Weigert, C. (2018). The effect of differentiation and TGFβ on mitochondrial respiration and mitochondrial enzyme abundance in cultured primary human skeletal muscle cells. Sci. Rep. *8*, 737. https://doi.org/10.1038/s41598-017-18658-3.
15. Shintaku, J., Peterson, J.M., Talbert, E.E., Gu, J.M., Ladner, K.J., Williams, D.R., Mousavi, K., Wang, R., Sartorelli, V., and Guttridge, D.C. (2016). MyoD regulates skeletal muscle oxidative metabolism cooperatively with alternative NF-κB. Cell Rep. *17*, 514–526. https://doi.org/10.1016/j.celrep.2016.09.010.
16. Wagatsuma, A., and Sakuma, K. (2013). Mitochondria as a potential regulator of myogenesis. Sci. World J. *2013*, 593267. https://doi.org/10.1155/2013/593267.
17. Rochard, P., Rodier, A., Casas, F., Cassar-Malek, I., Marchal-Victorion, S., Daury, L., Wrutniak, C., and Cabello, G. (2000). Mitochondrial activity is involved in the regulation of myoblast differentiation through myogenin expression and activity of myogenic factors. J. Biol. Chem. *275*, 2733–2744. https://doi.org/10.1074/jbc.275.4.2733.
18. Seyer, P., Grandemange, S., Busson, M., Carazo, A., Gamaléri, F., Pessemesse, L., Casas, F., Cabello, G., and Wrutniak-Cabello, C. (2006). Mitochondrial activity regulates myoblast differentiation by control of c-Myc expression. J. Cell. Physiol. *207*, 75–86. https://doi.org/10.1002/jcp.20539.
19. Bhattacharya, D., and Scimè, A. (2020). Mitochondrial function in muscle stem cell fates. Front. Cell Dev. Biol. *8*, 480. https://doi.org/10.3389/fcell.2020.00480.
20. Chan, D.C. (2020). Mitochondrial Dynamics and its Involvement in Disease.
21. Frezza, C., Cipolat, S., Martins de Brito, O., Micaroni, M., Beznoussenko, G.V., Rudka, T., Bartoli, D., Polishuck, R.S., Danial, N.N., De Strooper, B., and Scorrano, L. (2006). OPA1 controls apoptotic cristae remodeling independently from mitochondrial fusion. Cell *126*, 177–189. https://doi.org/10.1016/j.cell.2006.06.025.
22. Cogliati, S., Frezza, C., Soriano, M.E., Varanita, T., Quintana-Cabrera, R., Corrado, M., Cipolat, S., Costa, V., Casarin, A., Gomes, L.C., et al. (2013). Mitochondrial cristae shape determines respiratory chain supercomplexes assembly and respiratory efficiency. Cell *155*, 160–171. https://doi.org/10.1016/j.cell.2013.08.032.
23. Patten, D.A., Wong, J., Khacho, M., Soubannier, V., Mailloux, R.J., Pilon-Larose, K., MacLaurin, J.G., Park, D.S., McBride, H.M., Trinkle-Mulcahy, L., et al. (2014). OPA1-dependent cristae modulation is essential for cellular adaptation to metabolic demand. EMBO J. *33*, 2676–2691. https://doi.org/10.15252/embj.201488349.
24. Spiegel, R., Saada, A., Flannery, P.J., Burté, F., Soiferman, D., Khayat, M., Eisner, V., Vladovski, E., Taylor, R.W., Bindoff, L.A., et al. (2016). Fatal infantile mitochondrial encephalomyopathy, hypertrophic cardiomyopathy and optic atrophy associated with a homozygous OPA1 mutation. J. Med. Genet. *53*, 127–131. https://doi.org/10.1136/jmedgenet-2015-103361.
25. Lenaers, G., Hamel, C., Delettre, C., Amati-Bonneau, P., Procaccio, V., Bonneau, D., Reynier, P., and Milea, D. (2012). Dominant optic atrophy. Orphanet J. Rare Dis. *7*, 46. https://doi.org/10.1186/1750-1172-7-46.
26. Romanello, V., and Sandri, M. (2021). The connection between the dynamic remodeling of the mitochondrial network and the regulation of muscle mass. Cell. Mol. Life Sci. *78*, 1305–1328. https://doi.org/10.1007/s00018-020-03662-0.
27. Leduc-Gaudet, J.P., Hussain, S.N.A., Barreiro, E., and Gouspillou, G. (2021). Mitochondrial Dynamics and Mitophagy in Skeletal Muscle Health and Aging. Int. J. Mol. Sci. *22*, 8179. https://doi.org/10.3390/ijms22158179.
28. Hood, D.A., Memme, J.M., Oliveira, A.N., and Triolo, M. (2019). Maintenance of Skeletal Muscle Mitochondria in Health, Exercise, and Aging. Annu. Rev. Physiol. *81*, 19–41. https://doi.org/10.1146/annurev-physiol-020518-114310.
29. De Palma, C., Falcone, S., Pisoni, S., Cipolat, S., Panzeri, C., Pambianco, S., Pisconti, A., Allevi, R., Bassi, M.T., Cossu, G., et al. (2010). Nitric oxide inhibition of Drp1-mediated mitochondrial fission is critical for myogenic differentiation. Cell Death Differ. *17*, 1684–1696. https://doi.org/10.1038/cdd.2010.48.
30. Kim, B., Kim, J.S., Yoon, Y., Santiago, M.C., Brown, M.D., and Park, J.Y. (2013). Inhibition of Drp1-dependent mitochondrial division impairs myogenic differentiation. Am. J. Physiol. Regul. Integr. Comp. Physiol. *305*, R927–R938. https://doi.org/10.1152/ajpregu.00502.2012.
31. Yasuda, T., Ishihara, T., Ichimura, A., and Ishihara, N. (2023). Mitochondrial dynamics define muscle fiber type by modulating cellular metabolic pathways. Cell Rep. *42*, 112434. https://doi.org/10.1016/j.celrep.2023.112434.
32. Pereira, R.O., Tadinada, S.M., Zasadny, F.M., Oliveira, K.J., Pires, K.M.P., Olvera, A., Jeffers, J., Souvenir, R., Mcglauflin, R., Seei, A., et al. (2017). OPA1 deficiency promotes secretion of FGF21 from muscle that prevents obesity and insulin resistance. EMBO J. *36*, 2126–2145. https://doi.org/10.15252/embj.201696179.
33. Tezze, C., Romanello, V., Desbats, M.A., Fadini, G.P., Albiero, M., Favaro, G., Ciciliot, S., Soriano, M.E., Morbidoni, V., Cerqua, C., et al. (2017). Age-Associated Loss of OPA1 in Muscle Impacts Muscle Mass, Metabolic Homeostasis, Systemic Inflammation, and Epithelial Senescence. Cell Metabol. *25*, 1374–1389.e6. https://doi.org/10.1016/j.cmet.2017.04.021.
34. Tezze, C., Amendolagine, F.I., Nogara, L., Baraldo, M., Ciciliot, S., Arcidiacono, D., Zaramella, A., Masiero, G., Ferrarese, G., Realdon, S., et al. (2023). A combination of

metformin and galantamine exhibits synergistic benefits in the treatment of sarcopenia. JCI Insight *8*, e168787. https://doi.org/10.1172/jci.insight.168787.

35. Herkenne, S., Ek, O., Zamberlan, M., Pellattiero, A., Chergova, M., Chivite, I., Novotná, E., Rigoni, G., Fonseca, T.B., Samardzic, D., et al. (2020). Developmental and Tumor Angiogenesis Requires the Mitochondria-Shaping Protein Opa1. Cell Metabol. *31*, 987–1003.e8. https://doi.org/10.1016/j.cmet.2020.04.007.
36. Zamberlan, M., Boeckx, A., Muller, F., Vinelli, F., Ek, O., Vianello, C., Coart, E., Shibata, K., Christian, A., Grespi, F., et al. (2022). Inhibition of the mitochondrial protein Opa1 curtails breast cancer growth. J. Exp. Clin. Cancer Res. *41*, 95. https://doi.org/10.1186/s13046-022-02304-6.
37. Noguchi, M., Kohno, S., Pellattiero, A., Machida, Y., Shibata, K., Shintani, N., Kohno, T., Gotoh, N., Takahashi, C., Hirao, A., et al. (2023). Inhibition of the mitochondria-shaping protein Opa1 restores sensitivity to Gefitinib in a lung adenocarcinomaresistant cell line. Cell Death Dis. *14*, 241. https://doi.org/10.1038/s41419-023-05768-2.
38. Lapuente-Brun, E., Moreno-Loshuertos, R., Acín-Pérez, R., Latorre-Pellicer, A., Colás, C., Balsa, E., Perales-Clemente, E., Quirós, P.M., Calvo, E., Rodríguez-Hernández, M.A., et al. (2013). Supercomplex assembly determines electron flux in the mitochondrial electron transport chain. Science *340*, 1567–1570. https://doi.org/10.1126/science.1230381.
39. Ikeda, K., Shiba, S., Horie-Inoue, K., Shimokata, K., and Inoue, S. (2013). A stabilizing factor for mitochondrial respiratory supercomplex assembly regulates energy metabolism in muscle. Nat. Commun. *4*, 2147. https://doi.org/10.1038/ncomms3147.
40. Cogliati, S., Calvo, E., Loureiro, M., Guaras, A.M., Nieto-Arellano, R., Garcia-Poyatos, C., Ezkurdia, I., Mercader, N., Vázquez, J., and Enriquez, J.A. (2016). Mechanism of super-assembly of respiratory complexes III and IV. Nature *539*, 579–582. https://doi.org/10.1038/nature20157.
41. Ludikhuize, M.C., and Rodríguez Colman, M.J. (2021). Metabolic Regulation of Stem Cells and Differentiation: A Forkhead Box O Transcription Factor Perspective. Antioxidants Redox Signal. *34*, 1004–1024. https://doi.org/10.1089/ars.2020.8126.
42. Sin, J., Andres, A.M., Taylor, D.J.R., Weston, T., Hiraumi, Y., Stotland, A., Kim, B.J., Huang, C., Doran, K.S., and Gottlieb, R.A. (2016). Mitophagy is required for mitochondrial biogenesis and myogenic differentiation of C2C12 myoblasts. Autophagy *12*, 369–380. https://doi.org/10.1080/15548627.2015.1115172.
43. Gottschalk, B., Madreiter-Sokolowski, C.T., and Graier, W.F. (2022). Cristae junction as a fundamental switchboard for mitochondrial ion signaling and bioenergetics. Cell Calcium *101*, 102517. https://doi.org/10.1016/j.ceca.2021.102517.
44. Pernas, L., and Scorrano, L. (2016). Mito-Morphosis: Mitochondrial Fusion, Fission, and Cristae Remodeling as Key Mediators of Cellular Function. Annu. Rev. Physiol. *78*, 505–531. https://doi.org/10.1146/annurev-physiol-021115-105011.
45. Baechler, B.L., Bloemberg, D., and Quadrilatero, J. (2019). Mitophagy regulates mitochondrial network signaling, oxidative stress, and apoptosis during myoblast differentiation. Autophagy *15*, 1606–1619. https://doi.org/10.1080/15548627.2019.1591672.
46. Hansen, J.M., Klass, M., Harris, C., and Csete, M. (2007). A reducing redox environment promotes C2C12 myogenesis: implications for regeneration in aged muscle. Cell Biol. Int. *31*, 546–553. https://doi.org/10.1016/j.cellbi.2006.11.027.
47. Bloemberg, D., and Quadrilatero, J. (2016). Effect of mitochondrial fission inhibition on C2C12 differentiation. Data Brief *7*, 634–640. https://doi.org/10.1016/j.dib.2016.02.070.
48. Balsa, E., Soustek, M.S., Thomas, A., Cogliati, S., García-Poyatos, C., Martín-García, E., Jedrychowski, M., Gygi, S.P., Enriquez, J.A., and Puigserver, P. (2019). ER and Nutrient Stress Promote Assembly of Respiratory Chain Supercomplexes through the PERK-eIF2α Axis. Mol. Cell *74*, 877–890.e6. https://doi.org/10.1016/j.molcel.2019.03.031.
49. García-Poyatos, C., Cogliati, S., Calvo, E., Hernansanz-Agustín, P., Lagarrigue, S., Magni, R., Botos, M., Langa, X., Amati, F., Vázquez, J., et al. (2020). Scaf1 promotes respiratory supercomplexes and metabolic efficiency in zebrafish. EMBO Rep. *21*, e50287. https://doi.org/10.15252/embr.202050287.
50. Calvo, E., Cogliati, S., Hernansanz-Agustín, P., Loureiro-López, M., Guarás, A., Casuso, R.A., García-Marqués, F., Acín-Pérez, R., Martí-Mateos, Y., Silla-Castro, J.C., et al. (2020). Functional role of respiratory supercomplexes in mice: SCAF1 relevance and segmentation of the Q. Sci. Adv. *6*, eaba7509. https://doi.org/10.1126/sciadv.aba7509.
51. Shiba, S., Ikeda, K., Horie-Inoue, K., Nakayama, A., Tanaka, T., and Inoue, S. (2017). Deficiency of COX7RP, a mitochondrial supercomplex assembly promoting factor, lowers blood glucose level in mice. Sci. Rep. *7*, 7606. https://doi.org/10.1038/s41598-017-08081-z.
52. Baldelli, S., Aquilano, K., and Ciriolo, M.R. (2014). PGC-1α buffers ROS-mediated removal of mitochondria during myogenesis. Cell Death Dis. *5*, e1515. https://doi.org/10.1038/cddis.2014.458.
53. Amati-Bonneau, P., Valentino, M.L., Reynier, P., Gallardo, M.E., Bornstein, B., Boissière, A., Campos, Y., Rivera, H., de la Aleja, J.G., Carroccia, R., et al. (2008). OPA1 mutations induce mitochondrial DNA instability and optic atrophy 'plus' phenotypes. Brain *131*, 338–351. https://doi.org/10.1093/brain/awm298.
54. Ahmed, S.T., Craven, L., Russell, O.M., Turnbull, D.M., and Vincent, A.E. (2018). Diagnosis and Treatment of Mitochondrial Myopathies. Neurotherapeutics *15*, 943–953. https://doi.org/10.1007/s13311-018-00674-4.
55. White, R.B., Biérinx, A.S., Gnocchi, V.F., and Zammit, P.S. (2010). Dynamics of muscle fibre growth during postnatal mouse development. BMC Dev. Biol. *10*, 21. https://doi.org/10.1186/1471-213X-10-21.
56. Varanita, T., Soriano, M.E., Romanello, V., Zaglia, T., Quintana-Cabrera, R., Semenzato, M., Menabò, R., Costa, V., Civiletto, G., Pesce, P., et al. (2015). The OPA1-dependent mitochondrial cristae remodeling pathway controls atrophic, apoptotic, and ischemic tissue damage. Cell Metabol. *21*, 834–844. https://doi.org/10.1016/j.cmet.2015.05.007.
57. Del Dotto, V., Fogazza, M., Carelli, V., Rugolo, M., and Zanna, C. (2018). Eight human OPA1 isoforms, long and short: What are they for? Biochim. Biophys. Acta Bioenerg. *1859*, 263–269. https://doi.org/10.1016/j.bbabio.2018.01.005.
58. Gilkerson, R., De La Torre, P., and St Vallier, S. (2021). Mitochondrial OMA1 and OPA1 as Gatekeepers of Organellar Structure/Function and Cellular Stress Response. Front. Cell Dev. Biol. *9*, 626117. https://doi.org/10.3389/fcell.2021.626117.
59. MacVicar, T., and Langer, T. (2016). OPA1 processing in cell death and disease - the long and short of it. J. Cell Sci. *129*, 2297–2306. https://doi.org/10.1242/jcs.159186.
60. Sincennes, M.C., Wang, Y.X., and Rudnicki, M.A. (2017). Primary Mouse Myoblast Purification using Magnetic Cell Separation. Methods Mol. Biol. *1556*, 41–50. https://doi.org/10.1007/978-1-4939-6771-1_3.
61. Ross, J.M. (2011). Visualization of mitochondrial respiratory function using cytochrome c oxidase/succinate dehydrogenase (COX/SDH) double-labeling histochemistry. J. Vis. Exp. e3266. https://doi.org/10.3791/3266.
62. De Paepe, B., De Bleecker, J.L., and Van Coster, R. (2009). Histochemical methods for the diagnosis of mitochondrial diseases. Curr. Protoc. Hum. Genet. *Chapter 19*, Unit19.2. https://doi.org/10.1002/0471142905.hg1902s63.
63. Triolo, M., Wade, S., Baker, N., and Khacho, M. (2023). Evaluating mitochondrial length, volume, and cristae ultrastructure in rare mouse adult stem cell populations. STAR Protoc. *4*, 102107. https://doi.org/10.1016/j.xpro.2023.102107.
64. Khacho, M., Tarabay, M., Patten, D., Khacho, P., MacLaurin, J.G., Guadagno, J., Bergeron, R., Cregan, S.P., Harper, M.E., Park, D.S., and Slack, R.S. (2014). Acidosis overrides oxygen deprivation to maintain mitochondrial function and cell survival. Nat. Commun. *5*, 3550. https://doi.org/10.1038/ncomms4550.
65. Khacho, M., Clark, A., Svoboda, D.S., Azzi, J., MacLaurin, J.G., Meghaizel, C., Sesaki, H., Lagace, D.C., Germain, M., Harper, M.-E., et al. (2016). Mitochondrial Dynamics Impacts Stem Cell Identity and Fate Decisions by Regulating a Nuclear Transcriptional Program. Cell Stem Cell *19*, 232–247. https://doi.org/10.1016/j.stem.2016.04.015.

STAR★METHODS

KEY RESOURCES TABLE

REAGENT or RESOURCE	SOURCE	IDENTIFIER
Antibodies		
Anti-rabbit Tom20	ProteinTech	Cat# 11802-1-1AP; RRID: AB_2207530
Anti-rabbit OPA1	Abcam	Cat# ab42364; RRID:AB_944549
Anti-mouse GAPDH	Abcam	Cat# ab8245; RRID:AB_2107448
Anti-rabbit COX7A2L (SCAF1)	Abcam	CAT# ab222129; RRID: AB_3075341
Anti-rabbit COX7A2L	Proteintech	Cat# 11416-1-AP; RRID:AB_2245402
Anti-mouse Beta Actin	Millipore Sigma	Cat# A5316; RRID:AB_476743
Anti-mouse NDUFA9	Thermo Fischer Scientific	Cat# 459100; RRID:AB_2532223
Anti-mouse SDHA	Abcam	Cat # 14715; RRID:AB_301433
Anti-mouse UQCRC2	Abcam	Cat # 14745; RRID:AB_2213640
Anti-mouse ATP5A	Abcam	Cat# 14748; RRID:AB_301447
Anti-mouse MHCI	DSHB	Cat# BA-F8; RRID:AB_10572253
Anti-mouse MHCIIa	DSHB	Cat# SC-71; RRID:AB_2147165
Anti-mouse MHCIIb	DSHB	Cat# BF-F3; RRID:AB_2266724
Anti-mouse eMHC	DSHB	Cat# F1.652; RRID:AB_528358
Anti-rabbit Laminin	Abcam	Cat# ab11575; RRID:AB_298179
Goat anti-rabbit IgG (H+L) Alexa-Fluoro 488	Molecular Probes	Cat# A11008; RRID:AB_143165
Goat anti-mouse IgG (H+L) AlexaFluor 594	Invitrogen	Cat# A-11005; RRID:AB_2534073
Goat anti-rabbit IgG (H+L) AlexaFluor 647	Invitrogen	Cat# A-21244; RRID:AB_2535812
Goat Anti-Mouse IgG, Fcγ subclass 1 specific Biotin	Jackson ImmunoResearch	Cat# 115-065-205; RRID:AB_2338571
Cy3-Conjugated Streptavidin	Jackson ImmunoResearch	Cat# 016-160-084; RRID:AB_2337244
Goat anti-mouse IGg2 AlexaFluor 350	Thermo Fisher Scientific	Cat# A-21140; RRID:AB_2535777
Goat anti-mouse IgG1 AlexaFluor-488	Invitrogen	Cat# A-21121; RRID:AB_2535764
Horseradish peroxidase-conjugated Donkey anti-mouse (H+L)	Jackson ImmunoResearch	Cat# A16011; RRID:AB_2534685

(*Continued on next page*)

Continued

REAGENT or RESOURCE	SOURCE	IDENTIFIER
Horseradish peroxidase-conjugated Donkey anti-rabbit (H+L)	Jackson ImmunoResearch	Cat# A16023; RRID:AB_2534697
Alexa Fluor 488 Phalloidin	Thermo Fischer Scientific	A12379;
DAPI	Millipore Sigma	Cat# D9542;
Chemicals, peptides, and recombinant proteins		
Dulbecco's Modified Eagle's Medium	Wisent	Cat# 319-005-CL
HAMS F-10 Medium	Wisent	Cat# 318-050-CL
Phosphate buffered saline	Wisent	Cat# 311-010-CL
TrypLE Express	Gibco	Cat# 12605010
Penicillin-Streptomycin	Wisent	Cat# Wisent, 450-201-EL
Fetal Bovine Serum	Wisent	Cat# 080-150
Horse Serum	Wisent	Cat# 065-150
bFGF	Peprotech	Cat# 100-18B
MYLS22	Med Chem Express	Ca# HY-136446
Bovine serum albumin	Sigma	Cat# A4503
Triton x100	Sigma	Cat# 1002560820
Tamoxifen	Sigma	Cat# T5648
Cardiotoxin	Latoxan Laboratory	Cat# L8102
Lipofectamine 2000		
Oligomycin	Sigma	Cat# O4876-25MG
Critical commercial assays		
CellTiterGlo	Promega	G9241
Experimental models: Cell lines		
C2C12 myoblast cells	ATCC	Cat# CRL-1772; RRID:CVCL_0188
Primary myoblast cells	This paper	N/A
Experimental models: Organisms/strains		
OPA1-floxed-Pax7CreERT2	Baker et al., 2022[3]	N/A
C57BL/6 × Sv129	Varanita et al., 2015[56]	N/A
Oligonucleotides		
Opa1 Fwd 5′- CGACTTTGCCGAGGATAGCTT – 3′	Integrated DNA Technologies	Baker et al., 2022[3]
Opa1 Rvs 5′- CGTTGTGAACACACTGCTCTTT – 3′	Integrated DNA Technologies	Baker et al., 2022[3]
Scaf1 Fwd 5′ – GTTTAGCAGTTTCACGCAGAAG – 3′	Integrated DNA Technologies	Balsa et al., 2019[48]
Scaf1 Rvs 5′ – GGCAAATATGATAGGTGGTGC – 3′	Integrated DNA Technologies	Balsa et al., 2019[48]
Gapdh Fwd 5′ – TCGGTGTGAACGGATTTG – 3′	Integrated DNA Technologies	Baker et al., 2022[3]
Gapdh Rvs 5- GGTCTCGCTCCTGGAAGA – 3′	Integrated DNA Technologies	Baker et al., 2022[3]
β-Actin Fwd 5′- AAATCGTGCGTGACATCAAA – 3′	Integrated DNA Technologies	Baker et al., 2022[3]
β-Actin Rvs 5′- AAGGAAGGCTGGAAAAGAGC – 3′	Integrated DNA Technologies	Baker et al., 2022[3]
β-Tubulin Fwd 5′- GCACAATGGACTCAGTCAGG – 3′	Integrated DNA Technologies	Baker et al., 2022[3]
β-Tubulin Rvs 5′- CCCTTTGCCCAGTTATTTCC – 3′	Integrated DNA Technologies	Baker et al., 2022[3]
esiRNA-OPA1	Millipore Sigma	Cat# EMU010511
esiSCAF1	Millipore Sigma	Cat# EMU092741
Software and algorithms		
FIJI	NIH	https://fiji.sc
Prism GraphPad Version 10	GraphPad Software, Inc, 2016	https://www.graphpad.com/

(*Continued on next page*)

Continued

REAGENT or RESOURCE	SOURCE	IDENTIFIER
Other		
Immu-Mount Mounting Media	Epredia	Cat# 9990402
Pap Pen	Abcam	Cat# ab2601
Charged Glass Slides	Fisher Scientifi	Cat# 12-550-15
Cover Slip (24 × 50 mm)	Fisher Scientific	Cat# 12544E

RESOURCE AVAILABILITY

Lead contact

Further information and requests for resources and reagents should be directed to and will be fulfilled by the lead contact, Mireille Khacho (mkhacho@uottawa.ca).

Materials availability

This study did not generate new unique reagents.

Data and code availability

- All data reported in this paper will be shared by the lead contact upon request.
- This paper does not report original code.
- Any additional information required to reanalyze the data reported in this paper is available from the lead contact upon request.

EXPERIMENTAL MODEL AND STUDY PARTICIPANT DETAILS

Mouse models

All animal protocols were approved by the University of Ottawa's Animal Care Ethics Committee and adhered to the guidelines of the Canadian Council on Animal Care. All mice were housed and maintained at the Animal Care and Veterinary Service (ACVS) of the University of Ottawa.

As previously described in Baker et al., 2022[3] tamoxifen inducible and conditional adult muscle stem cell specific knockout of OPA1, OPA1-flox/flox mice were crossed with Pax7CreERT2 mice (OPA1-Pax7CreERT2, referred to as OPA1-KO). Wild-type mice were littermate mice that were OPA1-floxed but did not possess the CreERT2 recombinase (OPA1-WT). At 7-9 weeks of age, all mice received Tamoxifen (200 mg/kg) (Sigma T5648, 50 mg/mL dissolved in corn oil) administration via oral gavage for five consecutive days, followed by three days rest before any subsequent procedures were carried out. Specificity of OPA1 deletion in MuSCs was previously validated by our lab.[3] Male and female mice were used in this study.

Cell lines

C2C12 mouse skeletal muscle myoblast cells were obtained from American Type Culture Collection (ATCC, CRL-1772). Myoblasts were maintained in growth medium containing 20% (v/v) FBS (Wisent, 080-150) and 1% (v/v) penicillin-streptomycin solution (Wisent, 450-201-EL) in Dulbecco's modified Eagle's medium (DMEM; Wisent, 319-005-CL) with 4.5g/L glucose, L-glutamine, and sodium pyruvate. Myogenic differentiation was induced on confluent cells by changing to DMEM contain 2% (v/v) horse serum (Wisent, 065-150). Cells were grown in a humidified atmosphere at 37°C with 5% CO_2 and media was replaced every 2 days, were applicable.

Muscle primary cells were generated from the muscle stem cells of male, wild-type C57BL/6 × Sv129[56] mice using Magnetic Activated Cell Sorting (MACS) as previously described.[3] Briefly, following cervical dislocation, muscles from the mouse hindlimb were harvested, kept on 1xPBC on ice and minced. Subsequently, 5 mL of digestion enzyme cocktail containing 1% (w/v) Collagenase B (Roche 11088831001) and 0.4% (w/v) Dispase II (Roche 04942078001) was added. The muscle tissue and enzyme mixture were placed in a C-Tube (Miltenyi Biotec130-093-237) and subjected to dissociation using the Miltenyi MACS Octo-Dissociator with customized programs (SLICE_FACS), previously published.[60] The resultant slurry was then run through a 100 μm filter (Fisher Scientific 22363549) and cells were spun down at 600xg for 10 min. The resulting pellet was treated with 400 μL of red blood cell lysis buffer (Sigma R7757) for 30 sec, followed by addition of 10 mL PBS and centrifugation at 600xg for 5 min. Muscle stem cells were subjected to negative selection using the Satellite Stem Cell Isolation Kit (Miltenyi Biotec 130-104-268), followed by positive selection with an Anti-Alpha Integrin-7 antibody (Miltenyi Biotec 130-104-261). The resultant muscle stem cells were cultured on Matrigel-coated 10cm plates in growth media (HAM's F-10 media supplemented with 20% FBS (v/v), 1% penicillin-streptomycin (v/v) and 2.5ng/ μL bFGF). Following adherence and proliferation of cells to 70% confluency, primary myoblasts were purified by pre-plating to eliminate fibroblasts. All subsequent experiments were performed on this purified primary myoblast culture. Myogenic differentiation was induced on confluent cultured cells by changing to differentiation medium containing 2% horse serum. Cells were grown in a humidified atmosphere at 37°C with 5% CO2 and media was replaced every 2 days, when required.

METHOD DETAILS

Cardiotoxin injury

8-10 week old mice were subcutaneously injected with Buprenorphine (0.1 mg/Kg) and anesthetized by gas inhalation 30 min prior to Cardiotoxin (CTX) injection. 50μL of 10μM CTX (Latoxan Laboratory L8102) diluted in 1x phosphate buffered saline (PBS) was injected into the Tibialis Anterior (TA) muscle using a 28G-1/2 insulin syringe. The CTX-injected limb was used as the injured muscle, while the contralateral limb, that received no injection, was used as the uninjured contralateral control. Following the intervention, mice recovered in a cage with a heating pad and monitored for 24 hrs. Following 4, 7 or 21 days post injury (DPI), mice were euthanized by cervical dislocation. The TA muscles from both limbs were dissected, harvested, and prepared as described below.

Muscle fixation and sectioning

TA muscles were immediately dropped in 5 mL freshy prepared cold 2% (w/v) PFA (Sigma P6148) in 1xPBS and fixed for 30 min, shaking on ice. Next, fixed-TA muscles were washed twice with 5 mL of 1x PBS for 5 min, followed by two washes in 5 mL of 0.25 M glycine in 1x PBS for 10 min. TA muscles were then placed in 5 mL of 5% (w/v) sucrose in a 2.0mL centrifuge tube for 2 hrs at 4°C. TA muscles were subsequently transferred to a 1.5 mL centrifuge tube containing 20% sucrose (w/v) for 2-3 days at 4°C. The resultant TA tissue was embedded in Optimal Cutting Temperature (OCT) compound (VWR CA95057-838) and frozen in liquid nitrogen-cooled isopentane and immediately stored at -80°C. Tissue was sectioned in a cross-sectional orientation at a thickness of 14 μm using the HM525NX Cryostat (University of Ottawa Histology Core) at -28°C onto a charged slide (Fisher Scientific 12-550-15). Slides were stored at -80°C for further analysis.

Hematoxylin and Eosin staining and quantification of muscle regeneration

Tissue sections were stained with Hematoxylin and Eosin (H&E) according to standard procedure at the Histology Core Facility at the University of Ottawa. H&E-stained tissue sections were imaged using a Zeiss Axio Imager M2 microscope (CBIA Core, University of Ottawa). Images of entire tissue sections were obtained using the Zen tiling function, whereby single images taken at 20x magnification were stitched together. Quantification of myofiber numbers and size (cross-sectional area, CSA) were measured using the Fiji (ImageJ) software. Briefly, myofiber CSA was measured by tracing the perimeter of the fiber using the Fiji software drawing tool, and the minimum Ferret diameter was evaluated. The equation CSA = 3.14 * (minimum ferret diameter/2)^2 was used to calculate the CSA based on πr^2. To evaluate regenerated myofibers following CTX-injury, the number of centrally nucleated myofibers within a given region of interest (ROI) were counted and normalized to the ROI area (μm^2).

eMHC staining and quantification of muscle regeneration

Tissue sections were first subjected to antigen retrieval (UOttawa Histology Core) in sodium citrate buffer (10 μM sodium citrate, 0.05% (v/v) Tween-20, pH=6.0). Next sections were blocked in 3% (w/v) BSA diluted in 1x PBS for 1 hour. An anti-mouse eMHC primary antibody (DHSB F1.652-s) was diluted (1:15) in 3% BSA, and 40μL of diluted primary antibody was added to each tissue section and incubated overnight, in a humidified chamber, at 4°C. Next, sections were washed 5 x 2 minutes in 40mL of 1xPBS. Tissue sections were then incubated with 40ml of goat-anti mouse 594 secondary antibody (1:500; Invitrogen, A-11005) and DAPI (1:1000; Millipore Sigma, D9542) in 3% BSA for 40 minutes at room temperature in a dark, humified chamber. After being washed for 5 x 2 minutes in 40mL of 1xPBS, slides were mounted using Immumount (ThermoFisher 9990402) and stored overnight in the dark. Slides were subsequently stored at 4°C until imaged. Immunostained slides were imaged on a AxioObserver Z1 Epifluorescent microscope (CBIA Core) and quantified using the Fiji (ImageJ) software. For quantifications of cell populations, the number of eMHC positive myofibers were quantified within a given region of interest (ROI) and normalized to the total number of myofibers.

Muscle fiber type staining

Tissue sections were first subjected to antigen retrieval (UOttawa Histology Core) in sodium citrate buffer (10 μM sodium citrate, 0.05% (v/v) Tween-20, pH=6.0). Next sections were blocked in 2% BSA (w/v) in 1xPBS for 1 hour at room temperature. All antibodies described below were diluted in 2% BSA in 1xPBS, and all incubations took place in a dark, humidified, chamber. Primary antibodies against MHCI (1:75; BA-F8, DSHB), MHCIIa (1:500; SC-71, DSHB), MHCIIb (1:50; DSHB, BF-F3), and Laminin (1:1000; Abcam, 11575), were added to each tissue section, and incubated overnight 4°C. Sections were washed 3x5minutes in 1xPBS. Goat Anti-Mouse IgG, Fcγ subclass 1 specific Biotin (1:250; Jackson Immuno, 115-065-205) was added to tissue sections and incubated for 30 minutes at room temperature to bind specifically to the MHCIIa primary antibody. Following 3x5 minute washes in 1xPBS, secondary antibodies were incubated for 2 hours at room temperature. Secondary antibodies include Goat anti-mouse IGg2 AlexaFluor-350 (1:500; Invitrogen, A-21140), Goat Streptavidin-Cy3 (1:500; Jackson Immuno, 016-160-084), Goat anti-mouse IgG1 AlexaFluor-488 (1:500; Invitrogen, A-21121) and Goat anti-rabbit AlexaFluor-647 (Invitrogen, A-21244) to tag MHCI, MHCIIa, MHCIIb and Laminin, respectively. Images were captured on a Zeiss Axio Imager M2 microscope (CBIA Core, University of Ottawa). To ensure representative regions were sufficiently injured, serial sections were stained with Laminin and DAPI (1:1000) to confirm the presence of newly regenerated fibers (centrally nucleated).

Cytochrome C xidase (COX) and succinate dehydrogenase (SDH) staining

Immunohistochemical staining for the mitochondrial proteins cytochrome c oxidase (COX) and succinate dehydrogenase (SDH) in TA sections were conducted as previously described.[61,62] Briefly, tissue sections were dried at room temperature for 1 hour, placed into a humidified chamber and incubated with COX (1xDAB, 100 μM cytochrome c, 2mg bovine catalase in 0.1M PBS, pH=7.0) or SDH staining solution (1.5 μM NBT, 130 μM sodium succinate, 0.2 μM PMS, 1.0 μM sodium azide 0.1M PBS, pH-7.0) for 45 minutes at 37°C. Following incubation, slides were washed 3x5minutes in 0.1M PBS, and dehydrated using and ethanol gradient (70% ethanol x 2 for 2 minutes, 95% ethanol x 2 for 2 minutes and 100% ethanol for 10 minutes). Slides were then cleared with xylene and mounted using dibutyl phthalate polystyrene xylene (DPX). Images were taken on an EVOS Fl Auto2 microscope. Staining intensity was quantified only in newly regenerated fiber, and classified as low, intermediate or high activity.

siRNA-mediated knockdown of OPA1 and SCAF1

Cells were plated and the next day myoblasts were transfected with siOPA1 or siSCAF1 using Lipofectamine 3000 Transfection Reagent (Invitrogen, L3000001). Knockdown of OPA1 and SCAF1 was performed utilizing appropriate esiRNA (esiRNA-OPA1 EMU010511, esiSCAF1 EMU092741, Millipore Sigma) according to manufacturer guidelines. Lipofectamine 3000 was used as a Vehicle control. Cells were incubated for 48 hours prior to experiments.

Inhibition of OPA1 with MYLS22

To assess the influence of OPA1 inhibition on cell viability, mitochondrial length, metabolism and differentiation capacity of myoblasts, a novel OPA1 inhibitor, MYLS22 (Med Chem Express, HY-13644) was utilized.[35] In experiments evaluating cell viability and mitochondrial morphology in myoblasts, ~50% confluent cells were treated with 25 or 50μM of MYLS22 or DMSO, as a vehicle control, for 2 days. To assess the influence of OPA1 inhibition on differentiation, C2C12 and primary myoblast cells were plated in 6-well plates, until confluency was reached. At the time of differentiation induction, C2C12 cells were treated with 25 or 50 μM of the OPA1 inhibitor MYLS22 or DMSO, as a vehicle control. Primary muscle cells were treated with 25 μM or DMSO as a vehicle control. Cell culture media, supplemented MYLS22 or DMSO, was changed every 48 hours, were applicable.

Immunofluorescence staining

Following experimental treatment, cells were fixed using cold 4% paraformaldehyde and placed on an orbital shaker for 20 minutes at room temperature. Cells were then washed with 1xPBS (3x5 minutes). Cells were then simultaneously permeabilized and blocked in a blocking solution of 1% BSA (m/v) and 0.1% TritonX-100 (v/v), diluted in 1xPBS, for 20 minutes on an orbital shaker and washed with 1xPBS (3x5 minutes).To evaluate myotube fusion index, C2C12 and primary muscle cells were stained with Phalloidin-488 (1:1000; Thermofisher, A12379) and DAPI (1:1000) during the permeabilization and blocking period, while kept in the dark. Cells were then washed 3x5 minutes in 1xPBS for 5 minutes at room temperature. Images were taken at 20x for C2C12 cells and 10x for primary muscle cells, using a Zeiss-Axio Observer Epifluorescent Microscope. A minimum of 3 ROIs were imaged and quantified per experimental replicate. The average from each experimental replicate was used as a data point. Fusion index was calculated to demonstrate the extent of differentiation. Specifically, the number of nuclei in multinucleated (tri-nucleated, or more) myotubes fibers was divided by the total number of nuclei in each ROI. To assess mitochondrial morphology, glass coverslips were placed into 6-well plates. Following experimentation of C2C12 cells, coverslips were fixed, permeabilized and blocked. Mitochondria were stained with Tom20 (1:500; ProteinTech 11802-1-AP) in blocking solution and incubated overnight at 4°C in a humidified chamber. Glass slides were then washed 3x5 minutes in 1xPBS and incubated for 1 hour in Cy3 AffiniPure anti rabbit IgG (1:1000; Jackson Immuno, 711-165-152). DAPI (1:1000) was in the first of 3x5 minute 1xPBS washes at room temperature. Cells were mounted using Immu-Mount onto super-frost plus microscope slides and dried overnight in the dark prior to imaging. Cells were imaged on a LSM880 Confocal Microscope at the uOttawa Cell Biology Image Acquisition Core. Mitochondrial length was evaluated as previously described.[3,63–65] To measure SCAF1 levels and examine its localization to mitochondria, cells were plated on glass coverslips in 6-well plates. Following experiments, coverslips were fixed, permeabilized and blocked. Cells were then stained with anti mouse Cytochrome C (1:100; Santa Cruz, sc-13561) to mark the inner mitochondrial membrane, and anti rabbit SCAF1 (1:25; Abcam, ab222129) in blocking solution and incubated overnight at 4°C in a humidified chamber. Glass slides were then washed 3x5 minutes in 1xPBS and incubated for 1 hour in Cy3 AffiniPure donkey anti mouse IgG (1:400; Jackson Immuno, 711-165-152), goat anti-rabbit IgG (H+L) AlexaFluor-488 (1:400; Invitrogen, A-11008). DAPI (1:1000) was in the first of 3x5 minute 1xPBS washes at room temperature. Cells were mounted using Immu-Mount onto super-frost plus microscope slides and dried overnight in the dark prior to imaging. Cells were imaged on a LSM880 Confocal Microscope at the uOttawa Cell Biology Image Acquisition Core. Fluorescence intensity plots to qualitatively assess colocalization between Cytochrome C and SCAF1 was performed on Fiji Software using the RGB Profiler Plugin (https://imagej.nih.gov/ij/plugins/rgb-profiler.html).

Electron microscopy of myoblasts and differentiating myotubes

C2C12 cells were washed with ice cold 1xPBS and detached via TrypLE Express and collected into a 1.5mL centrifuge tube. Cells were then spun at 1200rpm for 5 minutes. The supernatant was removed and 500mL of EM fixative (2.5% glutaraldehyde solution in 0.2M Sodium Cacodylate buffer) was added and incubated at 4°C for 15 minutes. Next, the pellet was spun at 5000rpm for 8 minutes and the EM fixative was removed. Another 500mL of EM fixative was added, and samples were stored at 4°C. Samples were then sent to the Facility for Electron

Microscopy Research at McGill University for processing and sectioning. Electron micrographs were captured at the uOttawa TEM core facility using an JEOL JEM-1400Flash 120kv transmission electron microscope equipped with a GATAN 4K CMOS OneView digital camera and a Lab6 filament as emission source for enhanced contrast. Images of mitochondria were captured at 27,000-42,000x. Mitochondrial length and cristae parameters were measured using Fiji Software, as previously described.[63] Briefly, for each individual cristae the average diameter was measured from three representative regions. For each individual cristae junction width, the diameter was measured three times and the average was used.

ATP measurements

ATP levels were detected using the CellTiterGlo cell viability assay kit (Promega, G9241). First, adherent C2C12 cells were liberated with trypsin, placed in a 1.5mL microcentrifuge tube and spun at 4200 RPM for 2min. The resultant pellet was resuspended in 250-500ml of the appropriate cell culture media and subsequently plated in suspension (50μl) in a 96-well black transparent bottom microplate (LifeSciences, 781611). To block the activity of ATP Synthase and thus mitochondrial oxidative phosphorylation, a subset of cells were treated with 20μM Oligomycin and incubated for 30minutes in cell culture conditions. Finally, cells were incubated with 50μl of ATP-substrate, and luminescence was measured on a Biotek Synergy HT Microplate Reader. ATP concentrations were determined based on a standard curve analysis and normalized to the number of nuclei by counting DAPI on a tandem plate. Mitochondrial ATP contribution was quantified by taking the resultant difference between the -Oligomycin and +Oligomycin conditions and was normalized to cell number via a hematocytometer and Trypan Blue staining.

Assessing cellular respiration *in vitro*

Oxygen flux of proliferating myoblasts and whilst undergoing differentiation was assessed using a RESIPHER device (Lucid Scientific) with a 32-sensor lid compatible with a 96-well plate. C2C12 cells were seeded at 10,000 cells/well, whereas primary myoblasts were seeded at 20,000cells/per well. These cells were allowed to proliferate for 48 hours prior to the onset of differentiation. Oxygen consumption data were sampled every 15 min. For tracings of oxygen consumption rate (OCR) shown in Figures 2F, 2J, and 3L, all data points were plotted. For bar graphs shown in Figures 2G, 2K, and 3M, to quantify oxygen flux, the average OCR over the last hour of the indicated timepoint was used. Data in Figures 2F, 2G, 2I, 2J, and S2A–S2C, was normalized to the number of DAPI+ cells in parallel plates at the indicated timepoints. Data in Figures 3L and 3M, represent raw values.

RNA extraction and qPCR

RNA was isolated using Trizol-based extraction (Trizol, ThermoFisher 15596026). RNA extractions were performed under RNAse free conditions and preserved at -80°C. RNA was quantified using the Nanodrop 2000 spectrophotometer. qPCR was then performed using the Rotor-Gene SYBR RT-QPCR kit (Qiagen, 204174). Each sample was run in triplicate and normalized to GAPDH. To ensure that GAPDH was an appropriate housekeeping gene, gene expression changes were validated using Actin and/or Tubulin (Figures S2A, S3A, and S3B). Each gene was fitted to the appropriate standard curve and its concentration was subsequently analysed and represented. Primer sequences utilized include: OPA1 (F: CGACTTTGCCGAGGATAGCTT, R: CGTTGTGAACACACTGCTCTTG). SCAF1 (F: GTTTAGCAGTTTCACGCAGAAG, R: GGCA AATATGATAGGTGGTGCT) GAPDH (F: TCGGTGTGAACGGATTTG, R: GGTCTCGCTCCTGGAAGA), β-Actin (F: AAATCGTGCGTGA CATCAAA, R:AAGGAAGGCTGGAAAAGAGC) and β-Tubulin (F: GCACAATGGACTCAGTCAGG, R:CCCTTTGCCCAGTTATTTCC).

Protein analysis by western blot

Cells were washed with phosphate-buffered saline (PBS), lysed with 4% SDS in PBS, boiled for 5 minutes and the DNA was sheared by passage through a 26- gauge needle. Protein concentrations were determined using the DC Protein Assay (Biorad, 5000111). Equal amounts of protein (~20–30μg) were loaded and separated via SDS-PAGE and transferred onto PVDF membranes (Bio-Rad, 162-0177). Membranes were blocked with wash buffer (0.12% Tris-HCl, 0.585% NaCl, 0.1% Tween, pH 7.5) supplemented with 5% skim milk (w/v) at room temperature for 1 hour with gentle agitation. Membranes were then incubated with primary antibodies overnight at 4°C. Primary antibodies recognizing OPA1 (Abcam; ab42364), SCAF1 (Proteintech; 11416-1-AP), NDUFA9 (Thermo Fischer Scientific, 459100), SDHA (Abcam, 14715), UQCRC2 (Abcam, 14745), ATP5A (Abcam, 14748), MTCO1 (Invitrogen) GAPDH (Abcam; ab8245) were used. Ponceau staining was used to ensure equal protein loading for lysates. The next day, membranes were washed 3 × 5min in wash buffer and incubated for 1 hour at room temperature with the appropriate HRP-conjugated secondary antibody (Donkey anti-rabbit IgG (H+L) secondary antibody; A16023 or Donkey anti-mouse IgG (H+L) secondary antibody; A16011; Jackson ImmunoResearch) and subsequently washed 3×5 min in wash buffer. Protein density was visualized using Western Lightning Chemiluminescence Reagent Plus. Band densities were quantified by ImageJ software (NIH) and normalized to corresponding loading controls.

QUANTIFICATION AND STATISTICAL ANALYSIS

Student's unpaired t-tests were determined and computed with Excel. One-way and Two-way ANOVAs with respective post-hoc analyses were performed on Prism GraphPad Version 10. Specific statistical tests are indicated in figure legends.